Large eddy simulation of canonical atmospheric boundary layer flows with the spectral element method in Nek5000

L. Huusko[1], T. Mukha[2], L. L. Donati[1], P. P. Sullivan[3], P. Schlatter[4], G. Svensson[1,5]

[1]Departmet of Meteorology, SeRC, and Bolin Centre for Climate Research, Stockholm University, Stockholm, Sweden
[2]Computer, Electrical and Mathematical Sciences and Engineering Division, King Abdullah University of Science and Technology, Thuwal, Saudi Arabia
[3]National Center for Atmospheric Research, Boulder, Colorado, USA
[4]Institute of Fluid Mechanics, Friedrich-Alexander-Universität Erlangen-Nürnberg, Erlangen, Germany
[5]FLOW, Department of Engineering Mechanics, KTH Royal Institute of Technology, Stockholm, Sweden

Key Points:

- We introduce the spectral element solver Nek5000 for large eddy simulation of thermally stratified atmospheric boundary layer turbulence
- Statistics from Nek5000 simulations of stratified boundary layers are shown to be in good agreement with results from an established solver
- The paper may serve as a "recipe" for doing LES of the atmospheric boundary layer (ABL)

Corresponding author: Linnea Huusko, linnea.huusko@misu.su.se

Abstract

Simulation of turbulence in the atmospheric boundary layer is challenging due to the wide range of turbulent scales in the flow. To leverage the currently available computational power for high-resolution simulation of atmospheric turbulence, fluid solvers that scale well on large compute clusters are required. We present a new large eddy simulation (LES) framework based on the open-source solver Nek5000, which uses the highly parallelizable spectral element method for spatial discretization. We document the Nek5000 framework for LES of thermally stratified atmospheric boundary layers and present results from the solver for neutral, convective, and stably stratified boundary layers. To verify that the solver is capable of accurately representing important features of the atmospheric boundary layer, we compare our results to an established LES solver and find very good agreement in statistics as well as coherent structures. We also compare results with two different subgrid-scale models and conclude that one based on the subgrid-scale turbulent kinetic energy performs better together with the spectral element method.

Plain Language Summary

The atmospheric boundary layer is the part of the atmosphere closest to Earth's surface. The air flow in this layer is always turbulent and responds quickly to changes at the surface. Depending on the difference in temperature between the atmosphere and the surface, boundary layer turbulence has different characteristics. Because of this, and because there are both very large and very small turbulent eddies in the flow, simulating the turbulence is challenging. To accurately capture both the small and large eddies, the simulation must contain a large enough region of the lower atmosphere at a high resolution. We are developing a new framework for simulating air flow in the atmospheric boundary layer using a method called the spectral element method. This method is capable of utilising the currently available computational resources efficiently, enabling simulations at very high resolution. The framework is based on a code called Nek5000. In this paper we test our framework in four different cases. To verify that it is capable of capturing key aspects of different kinds of atmospheric boundary layers we compare our results to simulations with an established code. Our findings show good agreement in various statistical measures and snapshots of the turbulence.

1 Introduction

Numerical simulation of turbulence in the atmospheric boundary layer (ABL) is challenging due to the large range of scales present in the flow. Direct numerical simulation (DNS) of a turbulent flow, where all turbulent scales are explicitly resolved, requires a grid spacing on the order of the Kolmogorov scale. For typical atmospheric conditions, this means a grid spacing on the order of millimeters (e.g., Van Hooft et al., 2019), but since simulations of the ABL requires a domain size on the order of kilometers, this will not be feasible in the foreseeable future (e.g., Bou-Zeid, 2015). One solution is to resolve only the larger turbulent scales in the flow while relying on a subgrid-scale (SGS) model to represent the effects of the smallest scales on the flow. This approach is known as large eddy simulation (LES) and was first suggested by Smagorinsky (1963) and Lilly (1967), and since then a range of approaches to modeling the small scales has been suggested (Stoll et al., 2020).

Typically, LES of atmospheric flows is done on quasi-stationary cases of either convective or stably stratified boundary layers. There are a number of aspects that distinguish the ABL from other types of turbulent boundary layers, including the Coriolis effect and the thermal stratification. The lower boundary is represented as a rough surface, and temperature effects need to be considered in the formulation of the subgrid-scale model and in the application of the surface boundary condition. The effect of rotation leads to a wind direction that changes continuously with time at a given height, introducing non-stationarity even to problems with stationary forcing. These factors make it challenging to simulate even seemingly simple cases. For the convective boundary layer, convergence with increasing resolution has been demonstrated (Sullivan & Patton, 2011), but for the stable layer mesh convergence has proven elusive (e.g., Sullivan et al., 2016). Additional factors, such as time-varying boundary conditions, heterogeneous orography and surface forcing, or the impact of radiation and larger-scale atmospheric flow on the boundary layer, add additional complexity to the situation (e.g., Stoll et al., 2020; Van Hooft et al., 2019; Sullivan & McWilliams, 2010; Stiperski & Calaf, 2023; Mironov & Sullivan, 2024; Edwards et al., 2014; Mirocha & Kosović, 2010). Angevine et al. (2020) emphasize the importance of incorporating all relevant processes for realistic simulation of how the ABL changes throughout a diurnal cycle.

While there are numerous suggestions on how existing SGS models can be adjusted to obtain satisfactory representation of the large scales of turbulence in the ABL at coarse resolution, such adjustments typically require prior knowledge of the case to be simulated. At finer resolution, the impact from the SGS model becomes smaller and thus any assumptions made about the flow matter less. Our goal is therefore to leverage the currently available computational power as efficiently as possible to be able to simulate ABL flows at very fine resolutions, hopefully making it possible to eventually use a single SGS modeling framework to simulate the range of boundary layer types present in a diurnal cycle, minimizing the need for case-specific parameterization choices.

To do this, we use the open-source spectral element solver Nek5000 (Fischer et al., 2008). Nek5000 is well established as a DNS solver for canonical turbulent flow cases (e.g., El Khoury et al., 2013; Scheel et al., 2013) and here we document the additions we have made to the solver to use it for LES of atmospheric flows. The spectral element method (SEM; Patera, 1984) combines the accuracy of spectral methods with the flexibility of the finite element method (Fischer, 1997). The method is highly parallelizable, scales well on a large number of cores (e.g., Offermans et al., 2016), and allows for heterogeneous orography and non-uniform meshes.

Spectral element discretizations have been used for atmospheric modeling at different scales, ranging from large eddy simulation with Nek5000 (Chatterjee & Peet, 2015, 2017, focusing on wind energy applications and without considering thermal stratification) and with NekRS (e.g., Tombouldies et al., 2023; Tomboulides et al., 2024), to global

climate modeling in the Community Atmosphere Model (CAM, Dennis et al., 2012) and global weather forecasting in the newly developed Navy Environmental Prediction sysTem Utilizing a Nonhydrostatic Engine (NEPTUNE, Zaron et al., 2022; Müller et al., 2019), to name a few examples. A common motivation for using SEM is its scalability and performance on high performance computing clusters with a larger number of processors (e.g., Dennis et al., 2012; Zaron et al., 2022). Additionally, the flexibility of the grid allows for local mesh refinement (Offermans et al., 2020) and simulation of flow over orography. For Nek5000, our long-term goal is to develop an LES framework that can accurately simulate turbulence at high resolutions, and that can be used for a wide range of ABL cases including aerosol and cloud processes and heterogeneous orography. Nek5000 runs only on CPUs, but a new version of the code with GPU support, Neko, is currently under development (Jansson et al., 2024).

The aims of this paper are twofold. First, we document our LES solver Nek5000 and how it is set up to simulate atmospheric boundary layer flows. We discuss our choices in how the solver framework is set up and present results from four canonical cases (neutral, free convection, shear-convection and stably stratified boundary layers) in comparison with equivalent simulations with an established pseudospectral LES solver from the National Center for Atmospheric Research (NCAR) as described by Moeng (1984), Sullivan et al. (1994), and Sullivan and Patton (2011).

Second, we intend for the paper to serve as a "recipe" for performing large eddy simulation of atmospheric boundary layers. We emphasize key aspects of different ABL types and discuss what is required for adequate simulation. Furthermore, simulation of turbulence is key to research in both atmospheric and engineering sciences, and research on models and algorithms can benefit both communities. There are, however, differences in conventions and terminology that may make interdisciplinary work and exchange of results difficult. In this paper we mainly use ABL conventions, but we attempt to provide "translations" where it may be helpful for readers with an engineering background. As such, we hope that this paper may be useful to early career researchers of any background who are starting work on LES of the ABL.

2 Large Eddy Simulation

2.1 Governing Equations

The governing equations for LES of the dry atmospheric boundary layer are the filtered incompressible Navier-Stokes equations (e.g., Sullivan & Patton, 2011):

$$\frac{\partial \tilde{u}_i}{\partial t} + \tilde{u}_j \frac{\partial \tilde{u}_i}{\partial x_j} = -\frac{1}{\rho_0}\frac{\partial \tilde{p}}{\partial x_i} - \frac{\partial \tau_{ij}}{\partial x_j} + \delta_{i3} g \frac{\tilde{\theta} - \theta_0}{\theta_0} + f_c \varepsilon_{ij3}(\tilde{u}_j - U_{gj}), \tag{1}$$

$$\frac{\partial \tilde{u}_i}{\partial x_i} = 0, \tag{2}$$

$$\frac{\partial \tilde{\theta}}{\partial t} + \tilde{u}_i \frac{\partial \tilde{\theta}}{\partial x_i} = -\frac{\partial \tau_{\theta i}}{\partial x_i}, \tag{3}$$

where t is time, x_i is the spatial coordinate in the i direction, and u_i is the velocity component in the i direction. Throughout the text we base our notation and terminology on the conventions of the atmospheric sciences. We let $(x, y, z) = (x_1, x_2, x_3)$ and $(u, v, w) = (u_1, u_2, u_3)$. Assuming that the x coordinate is aligned with the East-West direction, the streamwise velocity u will be referred to as the zonal velocity. Then, the y coordinate is aligned with the North-South direction and the spanwise velocity v is referred to as the meridional velocity. The surface-normal (or wall-normal) direction, z, is referred to as vertical, and thus w is the vertical velocity. Furthermore, p is a pressure variable that includes the non-deviatoric part of τ_{ij}, θ is the potential temperature (which we will refer to simply as the temperature), θ_0 is a constant reference potential temperature, $g = 9.81$ m s^{-1} is the gravitational acceleration, $\rho_0 = 1$ kg m^{-3} represents density, f_c is the

Coriolis parameter, and U_{gi} is a geostrophic velocity, representing a pressure gradient, which is used to drive the flow. We use the alternating tensor ε_{ijk} and the Kroenecker delta δ_{ij}. The tilde denotes a spatially filtered quantity, and the total field of any variable ϕ is a sum of the filtered and subgrid-scale fields: $\phi = \tilde{\phi}+\phi''$. The deviatoric part of the subgrid-scale stress tensor $\tau_{ij} = \widetilde{u_i u_j} - \tilde{u}_i\tilde{u}_j$ and the subgrid-scale heat flux $\tau_{\theta i} = \widetilde{u_i\theta} - \tilde{u}_i\tilde{\theta}$ must be modeled. An overview of the models used for the present study is given in the following section, with details provided in the appendix. The Boussinesq approximation is used to incorporate buoyancy effects in the momentum equation (1). The molecular viscosity is assumed to be negligible due to the large Reynolds number of ABL flows.

2.2 Subgrid-Scale Modeling

The LES equation system requires specification of the subgrid stress τ_{ij} and heat flux $\tau_{\theta i}$ to close the system of equations. A common way of modeling the subgrid fluxes is through a linear eddy viscosity model (e.g., Moeng & Sullivan, 2015):

$$\tau_{ij} = -2K_m\tilde{S}_{ij}, \tag{4}$$

$$\tau_{\theta i} = -K_h\frac{\partial\tilde{\theta}}{\partial x_i}, \tag{5}$$

where K_m is an eddy viscosity (sometimes referred to as ν_t), $\tilde{S}_{ij} = 1/2(\partial\tilde{u}_i/\partial x_j + \partial\tilde{u}_j/\partial x_i)$ is the filtered rate of strain, and K_h (or ν_θ) is an eddy diffusivity. A simple version of the eddy viscosity model is the Smagorinsky-Lilly model (Smagorinsky, 1963; Lilly, 1967);

$$K_m = (C_S\Delta)^2|\tilde{S}|, \tag{6}$$

where C_S is the Smagorinsky constant, $\Delta = (\Delta_x\Delta_y\Delta_z)^{1/3}$ is a length scale based on the grid spacing, and $\tilde{S} = \sqrt{2\tilde{S}_{ij}\tilde{S}_{ij}}$. The eddy diffusivity is then related to the eddy viscosity through a subgrid-scale Prandtl number: $K_h = K_m/\mathrm{Pr}_{sgs}$. It should be noted that the filter scale does not necessarily need to be the same as the grid spacing, see for example the discussion of sub-filter scale modeling in (Stoll et al., 2020). In the present work, however, the filter scale is the same as the maximum grid spacing without any explicit filtering (see section 4 for a description of the grid spacing in Nek5000).

The Smagorinsky-Lilly model is commonly used to this day but has been found to be too dissipative (e.g., Pope, 2000). Numerous adjustments to the Smagorinsky-Lilly model have been suggested, ranging from selecting the model constant on a case-by-case basis (Deardorff, 1970, 1971, 1972; Matheou, 2016) to calculating it dynamically (Germano et al., 1991). A number of alternatives to the Smagorinsky-Lilly model have also been proposed, such as the Deardorff (1980) model based on the subgrid-scale turbulent kinetic energy (TKE) used by Moeng (1984) and later modified by Sullivan et al. (1994) to improve near-surface results. Chatterjee and Peet (2017) have done work to optimize the Smagorinsky-Lilly model for use in simulations of wall-bounded flows using SEM. For a more complete overview of subgrid-scale models used in LES of the atmospheric boundary layer we refer to Stoll et al. (2020).

As the NCAR LES, which we use as reference, uses the TKE-based model of Deardorff (1980) we implemented that model in Nek5000 for the present study to minimize the differences in the setup between the two codes. The Deardorff model, hereafter referred to as the TKE model, solves the prognostic equation for the subgrid-scale TKE and formulates an eddy viscosity based on that. This method takes the local temperature stratification into account, as a term for the local buoyancy production of TKE is present in the equation. Details of the implementation of the TKE model in Nek5000 are given in Appendix A. The NCAR LES also uses a two-part variant of the TKE model that gives

better agreement with Monin-Obukhov similarity theory (MOST) near the surface in horizontally homogeneous conditions (Sullivan et al., 1994). The two-part model is used for simulation of the neutral and stably stratified cases (see below; Berg et al., 2020; Sullivan et al., 2016). We did not implement the two-part TKE model in Nek5000 as preliminary results with the Deardorff model showed satisfactory agreement with the results from the NCAR model.

We have also used the Vreman (2004) model, which is a straightforward, constant-coefficient model that has found widespread use in the engineering community. It is an algebraic model designed to maintain the simplicity of the Smagorinsky-Lilly model while being less dissipative in near-wall regions and transitional flows (Vreman, 2004). The Vreman model does not include any information about the thermal stratification of the ABL, which means that in some cases it is not able to accurately capture the sharp temperature inversion that is capping the boundary layer (see Figure B1). To account for buoyancy effects, we have added a stability correction using the bulk Richardson number to the model (Moeng & Sullivan, 2015). Details on the implementation of the Vreman model in Nek5000 and the formulation of the stability corrected version are given in Appendix B, where we also show the effect of the correction. The term "Vreman model" will be used to refer to the stability corrected Vreman model (Equation B3). Although the TKE model gives the best comparison to the NCAR solver, we present results from simulations with the Vreman model to show sensitivity to the choice of SGS model.

It should be noted that regardless of what type of SGS model is used, a subgrid-scale Prandtl number will always appear. For the Vreman model we use a constant number that differs depending on the case. With the TKE model the value of the subgrid-scale Prandtl number is calculated locally depending on the stratification (see equation A3). A discussion of the current understanding of the turbulent Prandtl number in ABL flows can be found in Li (2019) and we will not comment further on the topic, but we note that this is a modelling choice that needs to be made in addition to the formulation of the eddy viscosity and diffusivity.

2.3 Monin-Obukhov Similarity Theory

As is commonly done for ABL flows we use a uniform resolution throughout the domain, and since the resolution is not sufficient to resolve the near-surface flow, a wall model is needed (e.g., Pope, 2000). The Vreman and TKE models described above are used to parameterize the subgrid-scale fluxes in the bulk of the domain, but at the lower boundary the stress and heat flux are given by (MOST; Monin & Obukhov, 1954). MOST gives the following relationships between the gradients of the total horizontal velocity, $V = \sqrt{u^2 + v^2}$, and temperature and the respective surface fluxes (e.g., Dyer, 1974):

$$\frac{\partial V}{\partial z} = \frac{u_*}{\kappa z}\phi_m\left(\frac{z}{L}\right), \tag{7}$$

$$\frac{\partial \theta}{\partial z} = -\frac{(\overline{w'\theta'})_s}{u_*\kappa z}\phi_h\left(\frac{z}{L}\right), \tag{8}$$

with the friction velocity $u_* = \sqrt{\tau_s/\rho_0}$, where τ_s is the value of τ_{ij} at the surface; and the Obukhov length $L = -\theta_0 u_*^3/(\kappa g(\overline{w'\theta'})_s)$, where $(\overline{w'\theta'})_s$ is the vertical heat flux at the surface. As is common for ABL simulations we let the von Kármán constant $\kappa = 0.40$ (e.g., Foken, 2006).

We use the Dyer (1974) formulations of the dimensionless shear and lapse rate, with

$$\phi_m(z) = \left(1 - 16\frac{z}{L}\right)^{-1/4}, \tag{9}$$

$$\phi_h(z) = \left(1 - 16\frac{z}{L}\right)^{-1/2} \tag{10}$$

for convective boundary layers and

$$\phi_m(z) = \phi_h(z) = 1 + 5\frac{z}{L} \tag{11}$$

for stably stratified boundary layers. Further details on how equations (7) and (8) are applied can be found in section 2.1 of Maronga et al. (2020).

Traditionally, the velocity and temperature used by the wall model are sampled in the first grid point above the surface. In the Nek5000 simulations we instead follow Maronga et al. (2020) and Kawai and Larsson (2012) and sample some distance z_s above the surface, at a point that is far enough from the surface to be outside the roughness sublayer (estimated to extend up to $50z_0$ above the surface, where z_0 is the roughness length for momentum) but still inside the surface layer (estimated to extend over the lowest 10% of the boundary layer depth, h). The value for z_s is chosen as 40 m for the neutral case, 25 m for the free convection case, 30 m for the shear-convective case, and 15 m for the stably stratified case.

3 Numerical Methods

3.1 Nek5000: Spectral Element Method

Nek5000 discretizes equations (1)–(3) using the spectral element method (SEM) introduced by Patera (1984). The domain is divided into a set of non-overlapping hexahedral elements. The method then requires that equations (1)–(3) are cast into weak form and then discretized on each element using the Galerkin method. The velocity is discretized on n+1 points per element in each direction, in a basis of nth-order Lagrange polynomial interpolants on Gauss-Lobatto-Legendre (GLL) quadrature points. The three-dimensional basis can be built as a tensor product of one-dimensional polynomials, which is central for the computational efficiency.

Two different algorithms for solving the governing equations, related to two different methods for discretizing the pressure field and coupling it to the velocity field, are available in Nek5000: the $\mathbb{P}_n$–$\mathbb{P}_n$ method that uses a n-th order polynomial for the pressure (Karniadakis et al., 1991) or the $\mathbb{P}_n$–$\mathbb{P}_{n-2}$ method that uses a polynomial order of $n-2$ (Maday & Patera, 1989). Both methods use a n-th order polynomial for the velocity. For the simulations in this study the $\mathbb{P}_n$–$\mathbb{P}_n$ method is used. The time integration is done semi-implicitly with third-order backward differentiation (BDF3) for viscous terms, and a third-order extrapolation scheme (EXT3) for non-linear terms and source terms (Karniadakis et al., 1991). The time step length is chosen adaptively to satisfy a given Courant-Friedrichs-Lewis (CFL) condition based on the maximum velocity relative to the spatial discretization. For the simulations in this study we use a target CFL number of 0.5. To avoid numerical instabilities, the 3/2 rule is used for dealiasing in the integration of the advective term (see Malm et al., 2013).

Equations (1) and (3) are integrated in time using a preconditioned conjugate gradient solver, and for the Poisson equation resulting from equation (2) a generalized minimal residual method solver is used. An additive overlapping Schwarz preconditioner is applied (Fischer, 1997), and the XX^T direct solver is used as the coarse-grid solver (Tufo & Fischer, 2001).

While the parallelizability of SEM means that it is possible to simulate large cases on big CPU clusters, parallelization on GPUs can allow for solution of even larger problems. Nek5000 can only be run on CPUs, but there is currently ongoing development of a new version of the code with GPU support: Neko (Jansson et al., 2024). A similar effort to modernize and build upon the Nek5000 framework has been made in NekRS (Fischer et al., 2022); a discussion of the differences between NekRS and Neko can be found in Jansson et al. (2024).

All simulations in the present paper were carried out with Nek5000 but our intention is to migrate our work on simulations of the ABL to Neko in the near future. Although the discussion in this paper refers to Nek5000, the purpose is to document the ability of SEM to simulate the ABL, and since both codes use the same discretization the conclusions should apply to both. Neko only has the $\mathbb{P}_n-\mathbb{P}_n$ version of the pressure-velocity coupling implemented; hence, we use that method for the Nek5000 simulations in this study.

3.2 NCAR LES: Pseudospectral Differencing

The code used as reference in the present work is the well established NCAR LES code first developed by Moeng (1984) with numerous modifications to simulate a variety of applications in the atmospheric and oceanic boundary layers over a wide range of stability (e.g., McWilliams & Restrepo, 1999; Sullivan et al., 2008; Sullivan & McWilliams, 2010; Sullivan & Patton, 2011; Sullivan et al., 2016). In dry atmospheric applications, the "flat version" of the NCAR LES integrates Equations (1)–(3) in time. The advective term in the momentum equation is written in rotational form (Moeng, 1984), while a flux conserving form is used for the advective term in the scalar (potential temperature) equation. The vertical velocity equation is integrated for the deviation of w from its horizontal mean value at each height. The flow variables are explicitly filtered at each time step, or dealiased, using the 2/3 rule (Moeng & Wyngaard, 1988).

The code utilizes well-established algorithms, to integrate Eqs. (1)-(3) forward in time. The horizontal differencing is pseudospectral and second-order finite differencing is used in the vertical direction. A compact fully-explicit third-order Runge-Kutta scheme (Spalart et al., 1991; Sullivan et al., 1996) is used for the time advancement where the time step is chosen to satisfy a CFL condition. This strategy allows for a wide variety of applications with different physical processes. The divergence free continuity equation (2) is discretely enforced by solving an elliptic pressure Poisson equation at each stage of the Runge-Kutta time stepping scheme. The code parallelization is based on the 2D domain decomposition described in Sullivan and McWilliams (2010) that uses custom built matrix transposes to carry out Fast Fourier Transforms and the tridiagonal solution of the pressure Poisson equation.

4 Description of Test Cases

Depending on the atmospheric conditions, the turbulence in the ABL has different characteristics that impose different requirements on the fluid solver to accurately simulate the flow. To verify that Nek5000 is able to capture the key aspects of the different types of flow, we simulate four different canonical test cases: an inversion capped neutral boundary layer (purely shear-driven turbulence, *neutral*), an inversion capped free convection (purely convection-driven turbulence, *free convection*), an inversion capped boundary layer driven by both shear and convection (*shear-convection*), and a stably stratified boundary layer (*stably stratified*). The neutral, free convection, and shear-convection cases are loosely based on cases studied by Berg et al. (2020), Schmidt and Schumann (1989), and Sullivan and Patton (2011), respectively. The stably stratified case follows the setup in the first GEWEX (Global Energy and Water cycle EXperiment) Atmospheric Boundary Layer Study (GABLS1, Beare et al., 2006). The setup for each case is described in Table 1 and values of physical parameters are given in Table 2. For each case we choose a resolution at which to perform a comparison between Nek5000 and the NCAR LES code, and for the neutral and shear-convective cases we also run Nek5000 at multiple resolutions to test the convergence of the statistics. Detailed investigation of the requirements for mesh convergence in the different cases has been carried out previously (Sullivan & Patton, 2011; Sullivan et al., 2016; Berg et al., 2020). As our aim is to verify that our code displays the expected behavior under increasing resolution, we limit our convergence

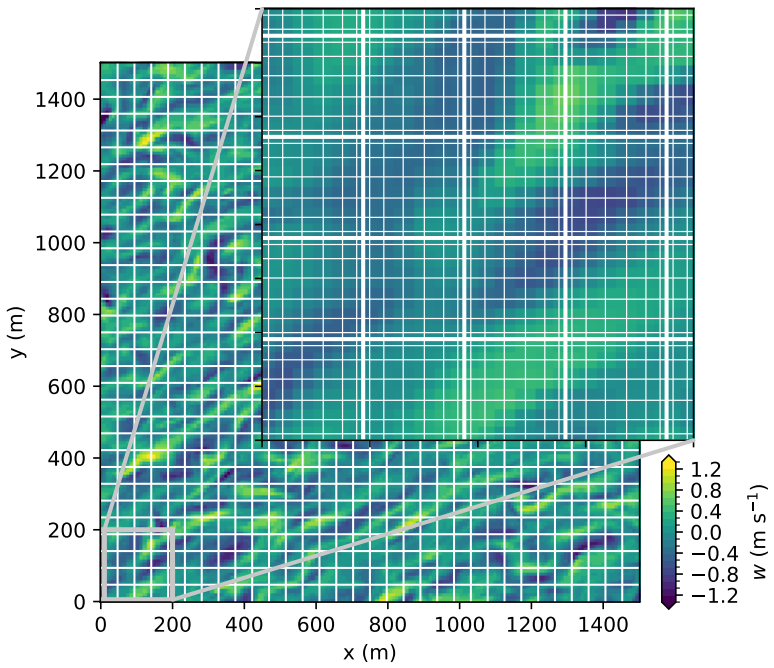

Figure 1. Illustration of a mesh with 32 elements in each direction in a horizontal cross section of a turbulent flow. In the inset box, thick white lines show element boundaries, while thin white lines show the GLL mesh; in the larger panel only the element boundaries are shown.

study to two cases and moderate resolutions. We emphasize that all cases presented in this paper are comparatively small and could easily be run using many existing LES codes; it is with future studies involving larger cases in mind that we have chosen to use Nek5000 and SEM as the foundation for our LES framework.

All simulations with Nek5000 are run in a domain of size $L_x \times L_y \times L_z$ with a resolution of $E_x \times E_y \times E_z$, where E denotes the number of elements in the spectral element discretization. SEM allows for two ways of refining the computational mesh: by increasing the number of elements and by increasing the polynomial order used for the solution. We use a polynomial order of 7 for all simulations, meaning that in each element there are 8 computational points. It should be noted that it is possible to use SEM with a lower-order polynomial, but for Nek5000 it is not recommended, as certain aspects of the numerics, such as the approximation of the mass matrix, benefit from a higher order. Test simulations of the shear-convection case show that first-order statistics are largely the same using order 3 and 7 and an equivalent number of total grid points, but profiles of second-order statistics are less smooth with order 3 (not shown).

The computational points within each element are not equidistantly spaced, as they are located according to GLL quadrature in each element, as illustrated in Figure 1 (the maximum GLL spacing for each simulation, $\Delta_{x,y}^{\max}$ in both horizontal directions and $\Delta_z^{\max}$ in the vertical, are given in Table 1). Therefore, in order to compare results to simulations with the NCAR LES of equivalent resolution, we assume that, for example, a Nek5000 simulation with 32 elements in each direction (giving $8 \times 32 = 256$ computation points) corresponds to a 256^3 grid mesh in the NCAR LES. For simplicity we will use the number of computation points, N, to refer to the resolution of a simulation throughout this paper, but the number of elements in each direction can always be obtained as $E = N/8$. For all simulations we use the same number of grid points N (and thus the same num-

Table 1. Case setup for simulations; number of grid points N in each direction; domain size ($L_x \times L_y \times L_z$); maximum GLL spacing in the horizontal, $\Delta_{x,y}^{\max}$, and vertical,$\Delta_z^{\max}$; and statistics interval T_{stat}.

Case	N	$L_x \times L_y \times L_z$ (km)	$\Delta_{x,y}^{\max}$ (m)	$\Delta_z^{\max}$ (m)	T_{stat} (s)
Neutral	256	$1.5 \times 1.5 \times 1.0$	9.8	6.5	$30000 - 36630$
Free convection	256	$5.0 \times 5.0 \times 2.0$	32.7	13.1	$10000 - 14000$
Shear-convection	256	$5.0 \times 5.0 \times 2.0$	32.7	13.1	$10000 - 14000$
Stably stratified	200	$0.4 \times 0.4 \times 0.4$	3.3	3.3	$28800 - 32400$

ber of elements E) in each direction. Note, however, that since the solution is matched at the boundaries between adjacent elements the number of unique degrees of freedom is smaller than $8E$. In Nek5000 it is easy to manipulate the mesh to include local refinement or grid stretching if desired, but for all simulations in the present study we use uniform elements throughout the domain.

For all simulations the boundary conditions are periodic on all lateral boundaries. At the top of the domain we specify fixed values for the velocity and temperature. The velocity is set to $(U_g, 0, 0)$, where the subscript g denotes the geostrophic velocity. The boundary condition for the temperature is set to the value that the initial profile for each case, described below, reaches at the top of the domain. At the surface boundary we use the surface stress obtained from MOST, as described in section 2.3. In the neutral and free convection cases we use equation (7) with $\phi_m = 1$ and in the shear-convective and stably stratified cases we use equations (9)-(10) and (11), respectively. For the neutral, free convection and shear-convection cases the surface heat flux is prescribed as a constant $Q_* = (\overline{w'\theta'})_s$ with the values in Table 2, while in the stably stratified case we instead specify a constant surface cooling rate $C_r = 0.25$ K h^{-1} and use equation (8) to compute the surface heat flux.

The initial condition for the temperature is a horizontally homogeneous profile defined by

$$\theta(z) = \begin{cases} \theta_0 & : 0 < z < z_1 \\ \theta_0 + \alpha(z - z_1) & : z_1 < z < z_2 \\ \theta_1 + \gamma(z - z_2) & : z > z_2, \end{cases} \tag{12}$$

where z_1, z_2 and θ_0 are chosen and θ_1 is calculated as $\theta_1 = \theta_0 + \alpha(z_2 - z_1)$ (θ_0 is the same as in equation (1)). All values are given in Table 2. An initial inversion zone is only used in the shear-convection case: for all other cases $z_2 = z_1$.

All simulations are forced with a constant geostrophic wind $U_{gi} = (U_g, 0, 0)$ where values for U_g for each case are given in Table 2. The roughness length for momentum and heat are set to $z_0 = z_h = 0.1$ m for all simulations. For the Coriolis parameter we use $f_c = 10^{-4}$ s^{-1} in all cases except the stable boundary layer, where we use $f_c = 1.39 \times 10^{-4}$ s^{-1}, in line with Beare et al. (2006).

To initiate turbulence we add a perturbation to the initial velocity conditions in the lowest 50% of the initial boundary layer according to

$$u_{\text{pert}} = \epsilon(\sin(ax)\sin(by) + \sin(cx)\sin(dy)), \tag{13}$$

$$v_{\text{pert}} = \epsilon(\sin(ax)\sin(by) + \sin(cx)\sin(dy)), \tag{14}$$

$$w_{\text{pert}} = -\epsilon(a\cos(ax)\sin(by) - c\cos(cx)\sin(dy)), \tag{15}$$

where $a = 5\pi/L_x, b = 7\pi/L_y, c = 40\pi/L_x, d = 40\pi/L_y$, and $\epsilon = 4$ m s^{-1}.

Table 2. Physical parameters for simulations: surface heat flux Q_*, geostrophic velocity U_g, reference potential temperature θ_0, and parameters z_1, z_2, α, and γ used in equation (12).

Case	Q_* (K m s^{-1})	U_g (m s^{-1})	θ_0 (K)	z_1 (m)	z_2 (m)	α (K m^{-1})	γ (K m^{-1})
Neutral	0	10	265	100	z_1	–	0.003
Free convection	0.06	0	300	600	z_1	–	0.003
Shear-convection	0.05	10	300	500	550	0.08	0.003
Stably stratified	–	8	265	100	z_1	–	0.01

The subgrid-scale TKE also requires an initial condition. The simulation is not sensitive to this condition since the TKE finds proper values as turbulence is spun up, but we follow Beare et al. (2006) and specify the initial condition for the subgrid TKE field as

$$e = \begin{cases} 0.4\,(1 - z/z_e)^3 & : 0 < z < z_e \\ 0 & : z > z_e, \end{cases} \tag{16}$$

with $z_e = 250$ m for the neutral and stably stratified cases and $z_e = 600$ m for the shear-convection and free convection cases. The boundary conditions for the subgrid TKE are set to $e = 0$ m^2 s^{-2} at $z = L_z$ and zero flux at the surface. See Appendix A for details on the formulation of the TKE-based subgrid-scale model.

The TKE model computes a subgrid-scale Prandtl number based on the local length scale (Appendix A) but for the Vreman model we prescribe $\mathrm{Pr}_{sgs} = 1$ in the stably stratified case, and $\mathrm{Pr}_{sgs} = 1/3$ in all other cases (Appendix B).

To avoid reflection of spurious gravity waves at the top of the domain it is common to use a radiation boundary condition, as formulated by Klemp and Durran (1983) and used in Sullivan and Patton (2011), Sullivan et al. (2016), and Berg et al. (2020). Lanzilao and Meyers (2023) compared the performance of the radiation condition and a damping layer in LES simulations of a wind park in a neutral boundary layer and found similar performance of the two methods for reducing gravity wave reflection, but noted that the damping layer has to be appropriately tuned to be effective. Based on the findings of Lanzilao and Meyers (2023) and on our own testing, we choose to use the damping layer that is already implemented in Nek5000 (Massaro et al., 2024), which is described in Appendix C.

Due to the stochastic nature of turbulence it is necessary to compute statistics to compare the results from the two solvers. Since all cases are horizontally homogeneous we approximate ensemble averaging with horizontal and temporal averaging. Identifying a suitable time window for averaging is, however, not straightforward as the simulations are only quasi-stationary. For each simulation we consider the time evolution of multiple quantities, such as the friction velocity and the velocity and temperature values at a few points in the domain, to assess whether turbulence is properly spun-up. We then choose an averaging window of multiple eddy turnover times $T_E = h/u_*$ for the neutral and stably stratified cases, or $T_E = h/w_*$ (where h is the boundary layer height and $w_* = (gQ_*h/\theta_0)^{1/3}$ is a vertical velocity scale) for the free convection and shear-convection cases. The averaging window T_{stat}, over which averages and higher-order statistics are computed for each simulation, is indicated in Table 1. Some variability in the statistics is expected due to the limited length of the averaging window; as the simulations are only quasi-stationary it is not possible to extend the averaging window to get better converged statistics. We use the notation $\phi = \overline{\phi} + \phi'$ where the overline indicates an average and the prime denotes the deviation from the average.

Table 3. Bulk quantities in simulations of the cases described in Tables 1 and 2, with different subgrid-scale models: boundary layer height h, defined as the height of the temperature variance maximum ($\overline{\theta'\theta'}$); friction velocity as used in the surface boundary condition (averaged in space over the whole domain); eddy turnover time, defined as h/u_* for the neutral and stably stratified cases and h/w_* for the free convection and shear-convection cases; all averaged over the statistics interval T_{stat} indicated in Table 1.

Case	h (m)	$h/\Delta_z^{\max}$	u_* (m s^{-1})	T_E (s)
Neutral Vreman	544	84	0.43	1351
Neutral TKE	563	87	0.43	1398
Free convection TKE	1188	91	–	896
Shear-convection Vreman	600	46	0.45	604
Shear-convection TKE	600	46	0.45	604
Stably stratified TKE	220	67	0.29	846

5 Results

In the evaluation of the performance of Nek5000 in the canonical ABL cases outlined in Tables 1 and 2, we have considered a number of variables, including vertical profiles of first, second, and third order statistics, snapshots of cross sections of the turbulent fields, and timeseries. Some statistics for all cases are presented in Table 3. In the interest of limiting the scope of this paper we here choose to present results from the neutral boundary layer in more detail, and then discuss the most interesting aspects of the other three cases. We then investigate mesh convergence and energy spectra in the neutral and shear-convection cases.

5.1 Neutral Case

Figure 2 shows the vertical profiles of $\overline{u}, \overline{v}$, and $\overline{\theta}$ in the neutral case. The figure shows very good agreement between Nek5000 and the NCAR solver, both when the Vreman and TKE SGS models are used in Nek5000. Both Nek5000 simulations capture the capping inversion as well as the zonal wind speed maximum (low level jet) just below the inversion. The boundary layer in the simulation with the stability corrected Vreman model is somewhat shallower and cooler (the boundary layer height is given in Table 3), but the overall shapes of the profiles match the reference well. To simulate a realistic atmosphere it is necessary that a solver accurately captures the boundary layer depth and the correct magnitude of the relevant variables, not just the correct shape of scaled profiles. Therefore, we choose to present unscaled values. Scaling the vertical axis with h would further improve the agreement between the three simulations. Note that the differences between the two Nek5000 simulations with different SGS models are larger than the differences between the simulations with Nek5000 and the NCAR LES which both use a TKE-based closure (Figure 2).

In the neutral boundary layer, the heat flux at the surface is zero, so the warming of the boundary layer compared to the initial condition is solely due to entrainment of warmer air across the inversion as the boundary layer grows deeper. Therefore, the cooler boundary layer temperature in the simulation with the Vreman model (Figure 2) could be due to the boundary layer developing more slowly in that simulation. However, Figure 3a, which shows the development of the friction velocity with time, indicates that

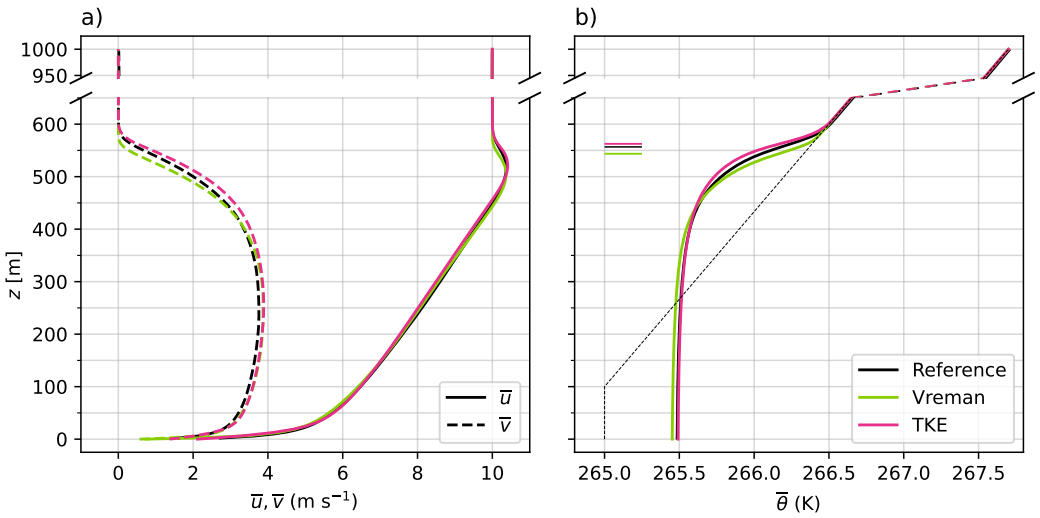

Figure 2. Vertical profiles of a) zonal (streamwise, solid lines) and meridional (spanwise, dashed lines) velocity, and b) temperature, in the neutral case, averaged over x and y and over the time span T_{stat} indicated in Table 1. Black lines show results from the reference simulation with the NCAR LES, colored lines show results from simulations with Nek5000 with two different SGS models (the stability corrected Vreman model and the TKE model, see section 2.2); this convention is used in all subsequent figures. In panel b, the short horizontal lines to the left indicate the boundary layer height, and the dashed black line indicates the initial temperature profile.

the turbulence by the surface develops very similarly in the two Nek5000 simulations (Table 3 confirms that the average u_* is statistically indistinguishable). Furthermore, the somewhat larger boundary layer height in the Nek5000 TKE model simulation (Table 3) is consistent through the whole timeseries (Figure 3), so it seems unlikely that the small discrepancies between the two Nek5000 simulations in Figure 2 would be due to the turbulence developing differently with time.

Figure 4 shows profiles of vertical momentum and heat fluxes in the neutral case. While there is very good agreement in the momentum fluxes between all three cases, the Vreman model has a smaller negative heat flux throughout most of the boundary layer. This explains the smaller mean ABL temperature seen in Figure 2, and is caused by a smaller subgrid-scale heat flux in the simulation with the Vreman model. It is noteworthy that the Nek5000 simulation with the TKE model has a substantially larger SGS heat flux than the reference simulation, despite the two simulations using the same SGS model and an equivalent resolution. The agreement in the total heat flux does, however, ensure that the average quantities in the neutral boundary layer develop similarly in the two simulations.

In the momentum flux, in the solution using the Vreman model there are "squiggles" in the first element above the surface, as seen in the box in Figure 4a. This seems to indicate some numerical instability. To investigate the structures present in the flow, Figure 5 shows snapshots of the flow field. Panels c and e show that the scales present in the flow close to the surface differ greatly between the two SGS models in Nek5000. The Vreman model retains small scales which are smoothed out by the TKE model. The scales present in the Vreman model with a resolution of 256^3 (Figure 5c) are similar to those in a simulation with the TKE model at 512^3 (Figure 5g), and to the reference sim-

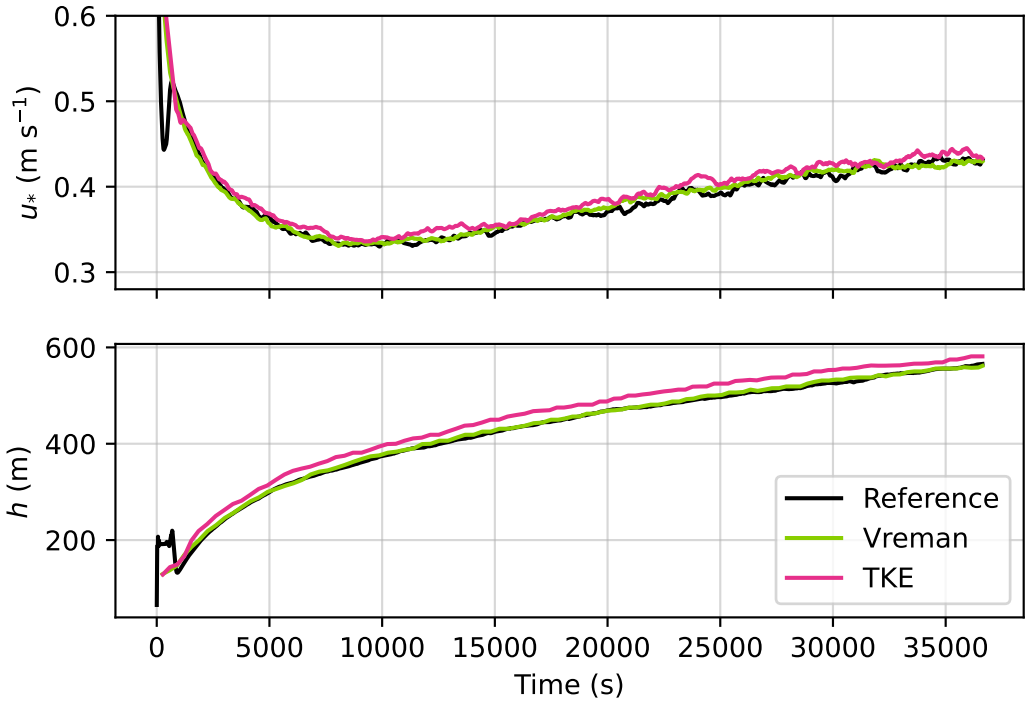

Figure 3. Time evolution of a) the friction velocity (u_*) and b) the boundary layer height (h) averaged over the domain, in the neutral case. The maximum value of the friction velocity at the start of the timeseries is approximately 1.2 m s^{-1} for the reference and 0.7 m s^{-1} for both Nek5000 simulations, but the values are not meaningful until later in the simulation when turbulence is properly spun up.

ulation with the TKE model in the NCAR LES (Figure 5a). That the TKE model seems to be more diffusive in Nek5000 than in the NCAR LES is not surprising as we use the maximum grid spacing, which is larger than the average grid spacing, to determine the length scale, which gives a larger eddy viscosity. This is, however, true also for the Vreman model in Nek5000.

In the middle of the mixed layer (Figure 5b, d, f) the flow fields are more similar in both codes, and with both SGS models in Nek5000. Nek5000 simulations take longer to complete with the Vreman model due to a larger number of iterations performed at each timestep. Figure B2 shows that in the shear-convection case the eddy viscosity is smaller with the Vreman model than the TKE model, particularly close to the surface; the behavior is very similar in the neutral case (not shown). The comparatively low eddy viscosity allows for small scales in the flow that are on the limit of what the current grid is capable of resolving, leading to some numerical instabilities. With increasing resolution, when there is less dependence on the SGS model to diffuse energy, this problem becomes less prominent (not shown). At the present resolution the larger eddy viscosity from the TKE model acts to smooth out the smallest structures, leading to smoother profiles in Figure 4a-b.

Figure 6b confirms that the simulation with the Vreman model does not display a smooth behavior close to the surface, presumably related to the low dissipation discussed above. The Nek5000 simulation with the TKE model performs better in this regard. All three profiles diverge more or less from the dashed line marking $\phi = 1$, but this is to be expected for LES (e.g., Brasseur & Wei, 2010). Figure 6a shows that the reference simulation captures the expected logarithmic behavior exceptionally well in the surface layer. It should be noted that the NCAR LES for this simulation uses the two-part version of the TKE model specifically designed to match the eddy viscosity to the similarity relationships in the surface layer (Sullivan et al., 1994).

In the inversion zone, small "spikes" can be seen in the heat flux profiles at element boundaries in the Nek5000 simulations with both SGS models (box in Figure 4c). SEM ensures continuity at element boundaries only in the solution itself, not in its derivatives. Discontinuities in the temperature gradient manifest as discontinuities in the heat flux, which is what we see in Figure 4c. The derivatives are expected to converge to a continuous solution at increasing resolution, but for the grid spacing used for LES the discontinuities are likely inevitable at coarse resolutions. It is conceivable that spikes in the vertical temperature gradient, in combination with the Boussinesq approximation, could cause undesired vertical acceleration, skewing the solution. Throughout the majority of the boundary layer the curves in Figure 4 are, however, smooth, and the small irregularities do not seem to noticeably affect the mean temperature profile.

The velocity variances (Figure 7) show good agreement throughout the boundary layer, with the exceptions of differences due to the somewhat shallower boundary layer, which disappear if the profiles are scaled by h (not shown), and somewhat larger values by the surface in the Vreman simulation, which are related to the large activity at small scales shown in Figure 5c.

The temperature variance (Figure 8) shows the most variation between the simulations with the largest values in the Nek5000 simulation with the TKE model, and the smallest values in the Nek5000 simulation with the Vreman model. The temperature variance is sensitive to the sharpness of the temperature inversion, and the exact shape of the mean temperature profile varies somewhat between the three simulations (Figure 2). Additionally, the comparatively short averaging time used due to the quasi-stationary nature of the case means that there is some variability in the higher-order statistics. Therefore, since there is no systematic shift between Nek5000 and the reference NCAR solver we consider the representation of the temperature variance by Nek5000 satisfactory.

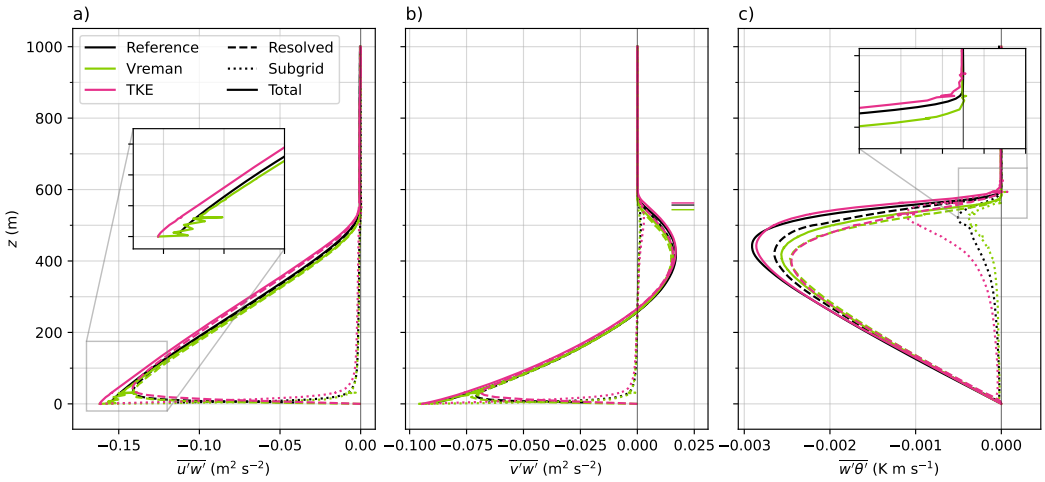

Figure 4. Vertical profiles of vertical fluxes of a) zonal momentum, b) meridional momentum, and c) temperature, in the neutral case. Inset boxes in panels a and c show total fluxes in higher detail in areas of interest. In panel b, the short horizontal lines to the right indicate the boundary layer height.

The second order statistics (Figures 4-8) indicate that Nek5000 is capable of capturing turbulent structures, at least as well as the NCAR solver. The agreement is better for the velocity statistics than for the temperature, perhaps indicating some sensitivity to how the temperature gradient is represented. To further investigate how the representation of the temperature structures affect the simulated flow we next consider the free convection case, where the turbulence is driven purely by convection.

5.2 Free Convection Case

As the free convection case involves no imposed horizontal wind, the mean profiles of the horizontal velocities show only noise and are thus not shown. This means that neither the MOST framework, used to calculate the surface fluxes (section 2.3), nor the stability corrected Vreman model are applicable, as they both involve division by the velocity gradients, which cannot be considered to be well defined in this case (regardless of what solver is used). Therefore, a simple rough wall is used for the surface boundary condition, and results are shown only for the TKE SGS model, although it should be noted that even this is not ideal since the mean velocity profiles are also zero and thus a logarithmic layer is not well defined.

Figure 9a shows that Nek5000 captures the correct shape of the mean temperature profile, although the mixed layer is somewhat warmer than in the reference case. The temperature variance has a similar maximum in both simulations (Figure 9b). The heat flux is also similar in the two simulations, although the Nek5000 profile has a slightly concave shape in the mixed layer, diverging somewhat from the expected linear shape.

The warmer mixed layer in Figure 9a could be caused by a slightly less sharp temperature inversion, allowing for entrainment of more warm air into the boundary layer. Figure 9c, however, shows that the maximum magnitude of the heat flux across the inversion is somewhat smaller in the Nek5000 simulation than in the reference. In simulations by Sullivan and Patton (2011) of a buoyancy driven boundary layer with weak shear, an increase in resolution caused a sharper temperature inversion accompanied by a weaker heat flux. Here, the thicker inversion layer in the Nek5000 simulation does not

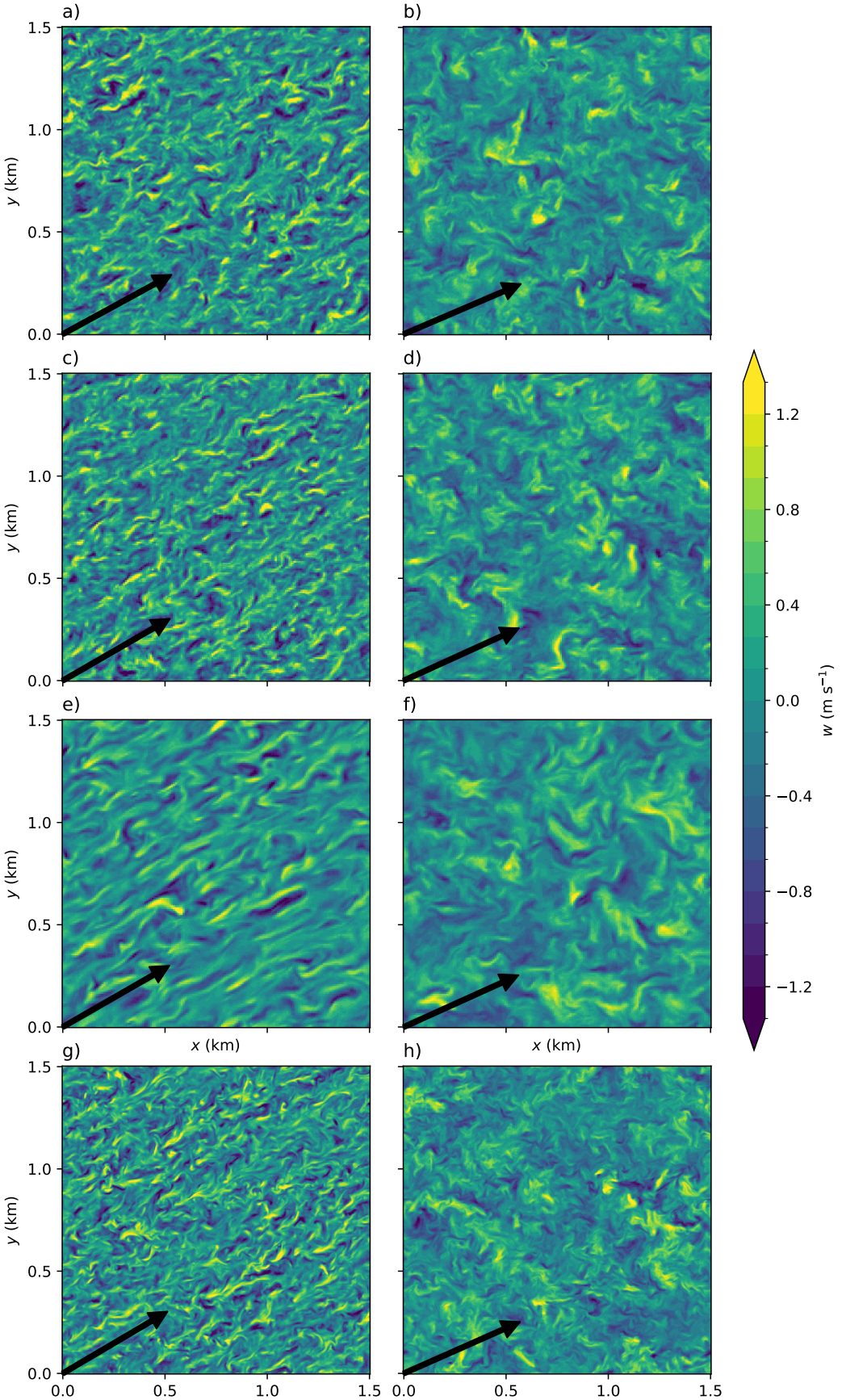

Figure 5. Horizontal slices at $t = 36630$ s of the vertical velocity field in the neutral case at approximately $z = 0.05h$ m (a, c, e, g) and $z = 0.5h$ m (b, d, f, h), from the NCAR LES (a-b), and from Nek5000 simulations with the stability corrected Vreman model (c-d) and the TKE model (e-f) with a resolution of 256^3, and the TKE model with a resolution of 512^3 (g-h). The

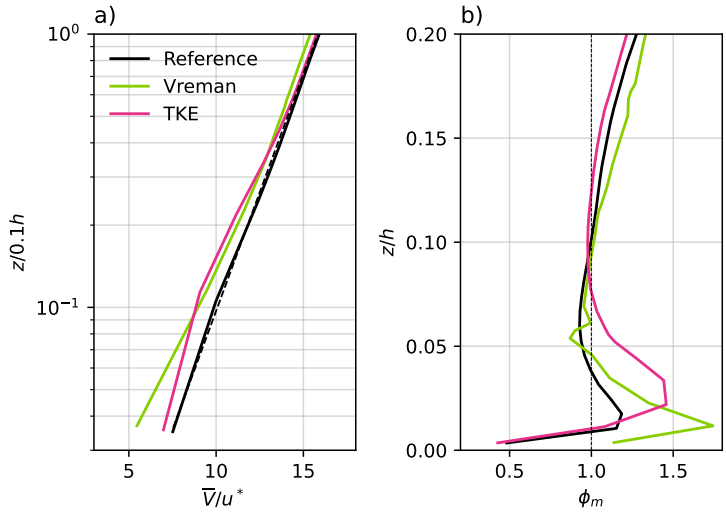

Figure 6. a) Nondimensionalized mean total velocity in the surface layer in the neutral case. The vertical axis has been normalized by $0.1h$, representing an estimate of the depth of the surface layer. The dashed black line shows the theoretical line predicted by equation (7) for a neutral boundary layer. b) Nondimensional wind shear as represented by the function ϕ_m (see equation (7)), which for a neutral boundary layer is expected to be unity. Here, the vertical axis is scaled by the boundary layer depth h.

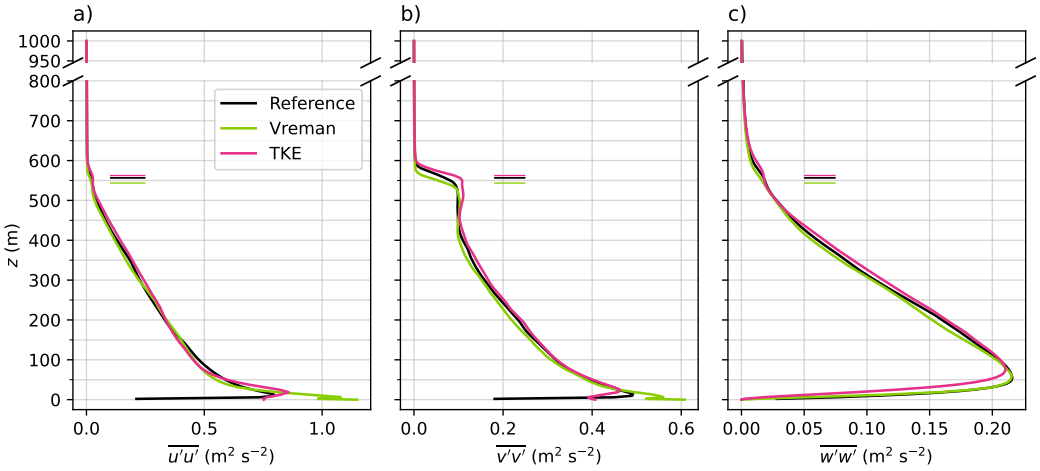

Figure 7. Vertical profiles of variances of a) zonal velocity, b) meridional velocity, and c) vertical velocity in the neutral case. The short horizontal lines to the left in each panel indicate the boundary layer height.

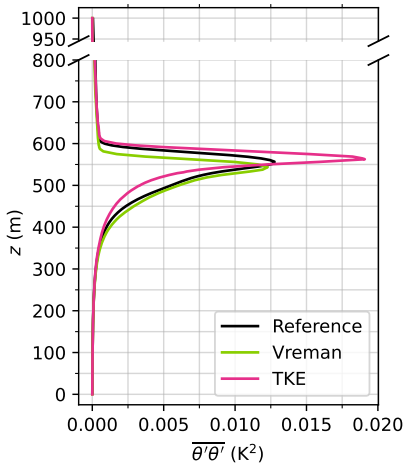

Figure 8. Vertical profile of the temperature variance in the neutral case.

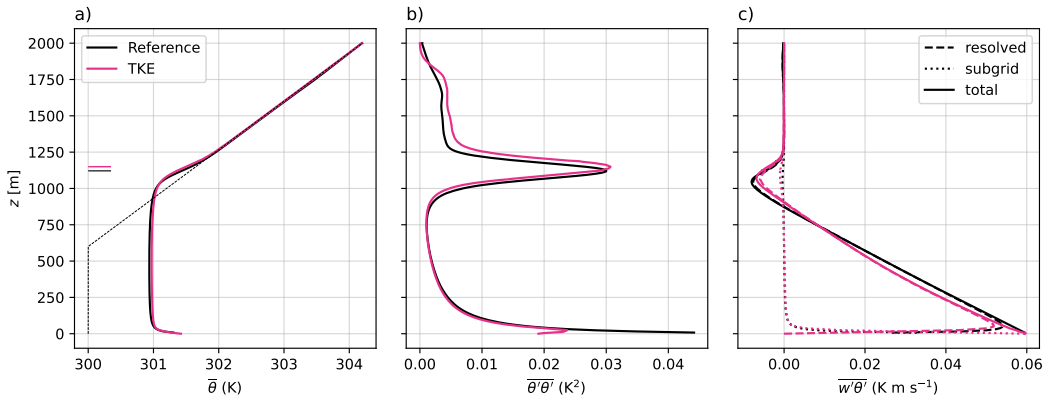

Figure 9. Vertical profiles of a) mean temperature, b) temperature variance, and c) vertical heat flux, in the free convection simulation. The statistics are computed over the time interval indicated in Table 1.

cause a larger heat flux. It is, however, clear from all panels of Figure 9 that Nek5000 simulates a less sharp temperature inversion, causing a deeper layer with a weaker negative heat flux and somewhat smaller temperature variance across the inversion.

5.3 Shear-convection Case

Studying the purely neutral and convective boundary layers is useful for understanding model behaviors, but the real atmosphere is always affected by both shear and buoyancy effects. We therefore turn next to the shear-convection boundary layer, which, while still idealized, involves more of the complexities of the real ABL.

In Figure 10a we see that there is good agreement with the reference data in both components of the wind, for both SGS models but particularly the TKE model. There is some difference in the magnitude of the wind in the mixed layer, but overall the magnitudes and the shape of the profiles are very similar in all three simulations. For the temperature (Figure 10b) there is very good agreement between all three profiles, and Table 3 confirms that the average boundary layer height is the same in the two Nek5000

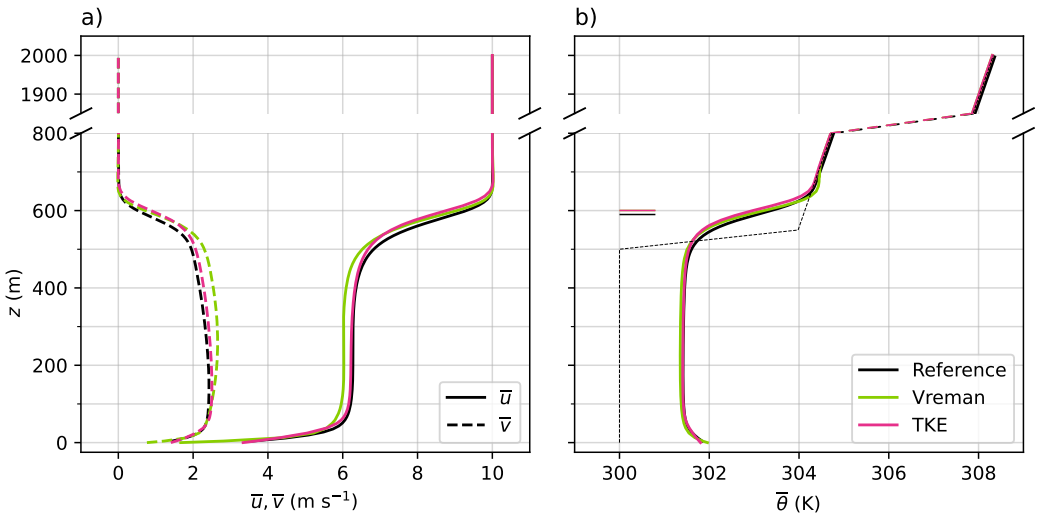

Figure 10. Vertical profiles of a) zonal (streamwise, solid lines) and meridional (spanwise, dashed lines) velocity, and b) temperature, in the shear-convection case, averaged over the time span indicated in Table 1. In panel b, the short horizontal lines to the left indicate the boundary layer height, and the dashed black line indicates the initial temperature profile.

simulations. In the Vreman simulation there is some overshoot in the temperature profile just above the inversion, although it should be noted that this overshoot is not present in simulations with the Vreman model at higher resolution (not shown).

Figure 11a-b shows good agreement in the profiles of the momentum flux. The inset box in Figure 11a highlights the fact that in the simulation with the Vreman model the flux profile is not smooth in the first element above the surface, similarly to the neutral case (Figure 4a). Snapshots of the shear-convection case shows the same behavior as in the neutral case, with smaller turbulent scales present in the flow close to the surface when using the Vreman model (not shown).

The heat flux profiles have discontinuities at the top of the inversion zone, as highlighted by the inset box in Figure 11c. The discontinuities are concentrated to the inversion zone where the temperature gradient changes quickly with height. In the shear-convection simulation with the Vreman model there is positive heat flux at the top of the boundary layer, causing an overshoot in the temperature profile just above the boundary layer in Figure 10. This behavior is not present in the simulation with the TKE model, indicating that the TKE model is better able to handle the temperature gradient in that region at the current resolution.

Furthermore, Figure 11c shows that there is very good agreement in the total heat flux profiles between the Nek5000 simulation with the TKE model and the reference simulation. As in the neutral case, there is some difference between the two solvers in how much of the heat flux is carried by the SGS model despite the resolution being equivalent.

The resolved vertical velocity skewness,

$$S_w = \frac{\overline{w^3}}{\overline{w^2}^{3/2}}, \tag{17}$$

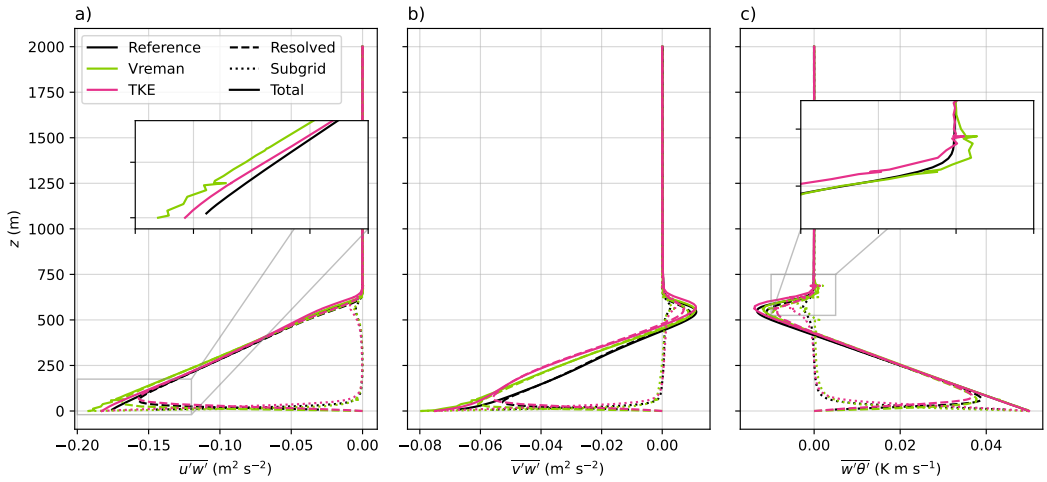

Figure 11. Vertical profiles of vertical fluxes of a) zonal momentum, b) meridional momentum, and c) temperature, in the shear-convection case. Inset boxes in panels a and c show total fluxes in higher detail in areas of interest.

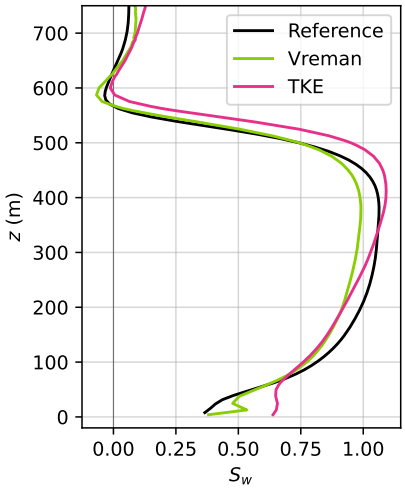

Figure 12. Vertical profile of resolved vertical velocity skewness in the shear-convection case.

is a key quantity in a convection-driven boundary layer as it contains information about the distribution of updrafts and downdrafts and about vertical transport (Sullivan & Patton, 2011; Moeng & Rotunno, 1990). Figure 12 displays good agreement between Nek5000 and the reference, showing that this third-order moment is represented in a similar way by both solvers. Above the boundary layer top the vertical velocity is very close to zero, and the skewness values are not meaningful due to the smallness of the denominator in equation (17).

5.4 Stably Stratified Case

The final case to consider is the stably stratified ABL, a case for which grid convergence has proven elusive at currently available grids (e.g., Sullivan et al., 2016; McWilliams et al., 2023). This case is by far the most expensive out of those simulated in this study,

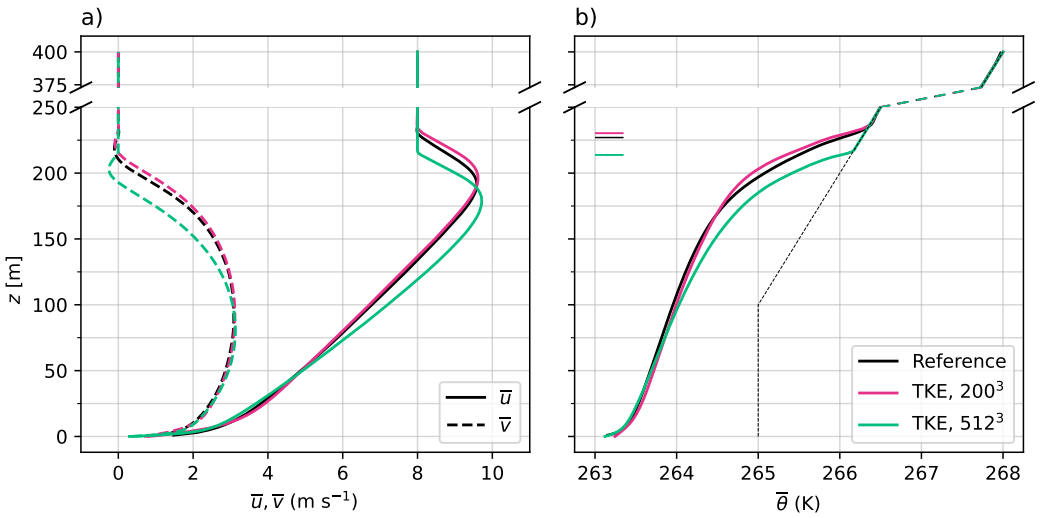

Figure 13. Vertical profiles of a) zonal (streamwise, solid lines) and meridional (spanwise, dashed lines) velocity, and b) temperature, in the stably stratified case, averaged over the time span indicated in Table 1. In panel b, the short horizontal lines to the left indicate the boundary layer height, and the dashed black line indicates the initial temperature profile.

so in the interest of limiting the use of computational resources we have simulated this case only with the TKE model. Fuka and Brechler (2011) used the Vreman model (without stability correction) to simulate the GABLS1 case with a finite volume solver and found that the model performed satisfactorily. They did, however, note a difference in the temperature gradient in the boundary layer compared to the models studied by Beare (2008).

The profiles of mean velocities and temperature (Figure 13) show good agreement with the reference at a resolution of 200^3 computation points (25^3 elements with SEM). Nek5000 successfully captures the low-level jet toward the top of the boundary layer, as well as the wind turning with height. The wind turning angle is 39° between the first level above the surface and the geostrophic wind, in line with Svensson and Holtslag (2009). The boundary layer is somewhat deeper compared to the reference case, but the difference is small compared to the range displayed by the models included in the intercomparison by Beare et al. (2006). Increasing the resolution leads to a shallower boundary layer, in line with results from Beare et al. (2006), Sullivan et al. (2016), and McWilliams et al. (2023). As it would be unlikely to provide any new information we did not perform any simulation at higher resolution than 512^3 computation points, but the difference between the two Nek5000 simulations in Figure 13 is in line with Figure 1 of Sullivan et al. (2016).

Sullivan et al. (2016) investigated in detail the spatial structures present in the stable boundary layer. Figure 14 confirms that the temperature fronts highlighted by Sullivan et al. (2016) are successfully represented in the Nek5000 simulations. We can see how the tilt of the fronts decreases toward the top of the boundary layer, as expected. At higher resolution (Figure 14b), smaller-scale structures are visible, and the behavior described by Sullivan et al. (2016) where the tilt of the fronts varies with the location along the x-axis is present.

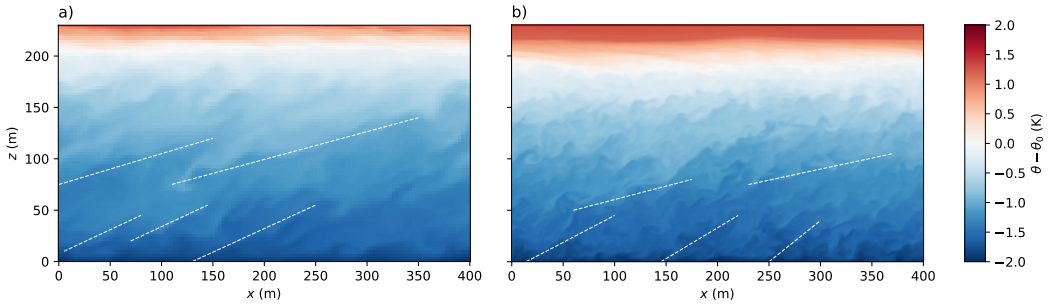

Figure 14. Visualization of temperature fronts in the stably stratified case: vertical cross sections at $y = 200$ m of the temperature field $(\theta - \theta_0)$ at $t = 9$ hours, from simulations with resolutions of a) 200^3 points, and b) 512^3 points. White lines have been added manually to indicate the location of a few strong temperature fronts in each case.

5.5 Mesh Convergence

As the spatial resolution is increased in an LES simulation the solution should become less dependent on the parameterized subgrid-scale motions, and thus, ideally, at some resolution become independent of the grid spacing. It should be noted that mesh convergence is not as straightforward for LES as it is for DNS. Implicit filtering means that the grid spacing is built into the solution and if the resolution gets too high some assumptions of the wall model are violated. Whether or not mesh convergence can actually be expected for wall-modelled LES is an active research topic (e.g., Hu et al., 2024). We do, however, still find it useful to investigate how the solution behaves under increased resolution in different boundary layers, and in particular to see how Nek5000 compares to the NCAR LES in this regard; a code that scales well to many processors is less useful if the mesh convergence is unsatisfactory.

When run at three different resolutions, the shear-convection case shows very good agreement in the temperature profile, aside from some minor differences by the surface as well as just above the inversion (Figure 15b). There is also very good agreement in the total heat flux (Figure 15c), where the primary difference between the three profiles is the proportion of the flux that is carried by the SGS model. This is in line with results from Sullivan and Patton (2011) who showed convergence in a similar shear-convective case with mesh resolutions of 256^3 and greater.

The wind speed profiles in Figure 15a show a decrease in $\overline{u}$ and an increase in $\overline{v}$ with increased resolution, corresponding to a decrease in the total mixed-layer wind speed but also involving an increase in the amount of wind turning with height. The diagnosed boundary layer height is the same with all three resolutions, and scaling the velocities with the friction velocity does not cause the profiles to collapse; therefore we choose to show unscaled profiles. The changes in the wind with resolution are likely related to changes in the dynamic stability at the point where the velocity field is sampled for the wall model. The boundary condition assumes a constant flux between the surface and the sampling point and the behavior in this region changes with resolution, thereby changing the boundary condition. Further investigation of this is outside the scope of the present study.

In the neutral case, where the temperature structure plays a smaller role, the convergence of the velocity profiles improves (Figure 16a). In this case, the vertical axes have been scaled with the boundary layer height as it varies substantially between the resolutions. Furthermore, the interval over which the statistics have been computed has been adapted to cover $20-25T_E$. For the mixed case this was not necessary as the eddy turnover

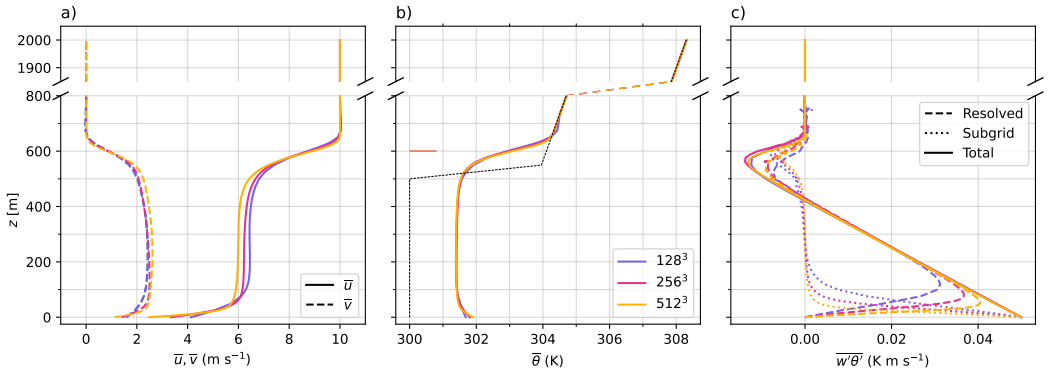

Figure 15. Profiles of a) zonal and meridional mean velocity, b) mean temperature, and c) vertical heat flux in the shear-convection case at three different resolutions ($128^3, 256^3$, and 512^3). The short horizontal lines to the right in panel b indicate the boundary layer height; the black dashed line shows the initial profile.

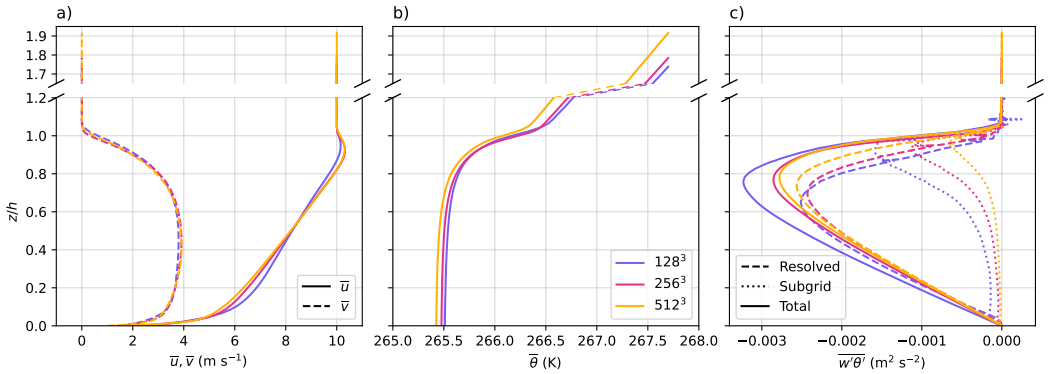

Figure 16. As Figure 15 but for the neutral case. The profiles have been scaled vertically with the boundary layer height, which is 575 m, 560 m, and 522 m, respectively, from low to high resolution.

time T_E is virtually identical regardless of the resolution, but in the neutral case it varies noticeably, indicating poor mesh convergence.

The differences between the three simulations, which are found mainly close to the top and the bottom of the boundary layer, are in line with results of Berg et al. (2020), who reported that their simulations were not fully converged despite using 1024^2 horizontal grid points. Therefore, we judge that our simulations are as close to convergence as can be expected at the current resolutions. The same conclusion can be drawn based on the mean temperature and heat flux (Figure 16b, c), which do show some variation with resolution, but the variations are very similar to those found by Berg et al. (2020). We refrain from performing costly simulations at higher resolution than the current 512^3 as it would not add much value to the aim of the present paper to document Nek5000 as a solver for ABL flows. For the same reason we do not perform a comprehensive convergence test of the stably stratified case but draw the conclusion based on Figure 13 that our simulations behave as expected at the current resolutions. For further investigation of the resolution dependence of the stable boundary layer we refer to Sullivan et al. (2016) and McWilliams et al. (2023).

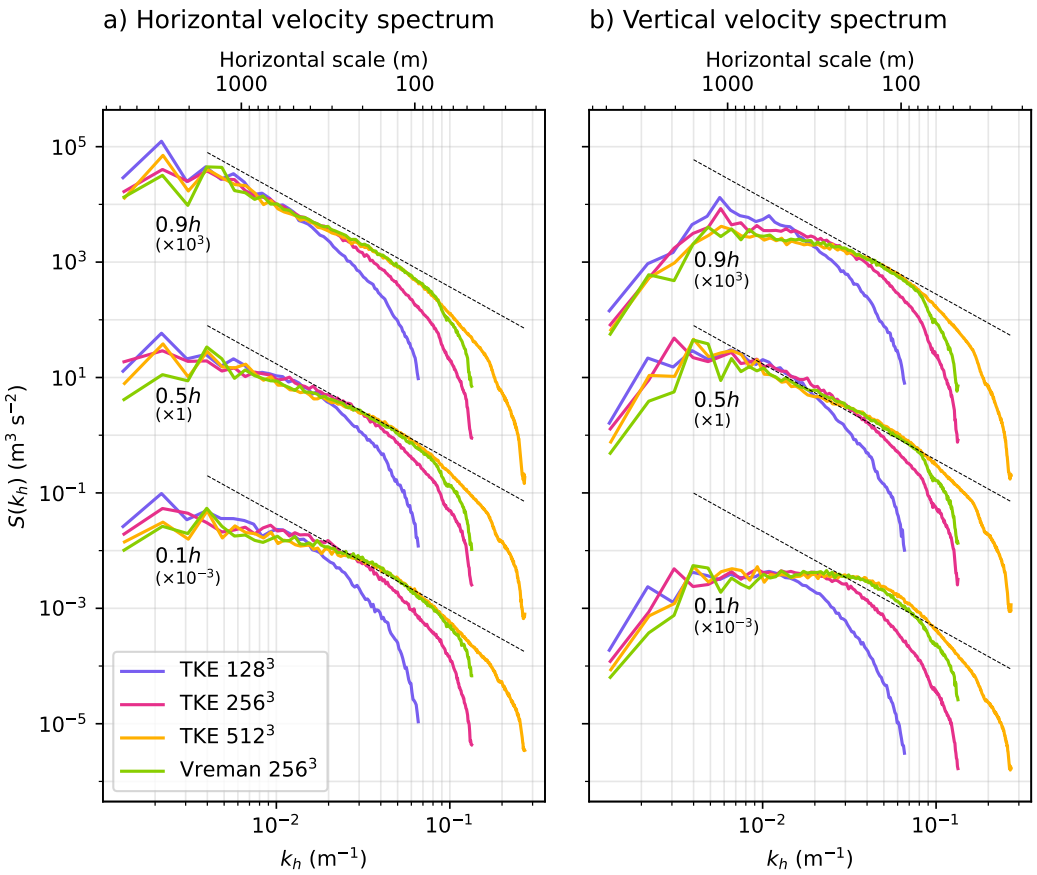

Figure 17. Energy spectral density as a function of the horizontal wavenumber $k_h = \sqrt{k_x^2 + k_y^2}$ in the shear-convection case for a) the total horizontal velocity $V = \sqrt{u^2 + v^2}$, and b) the vertical velocity w from simulations with the TKE model at three different resolutions and the Vreman model at one resolution, at three different heights; $0.9h, 0.5h$, and $0.1h$. The spectra have been scaled with the factors indicated for clarity. The dashed line shows the $-5/3$ slope.

5.5.1 Energy Spectral Density

Another way of investigating the impact the resolution has on the solution is through energy spectra, which we have computed according to the procedure described in Appendix D. The spectra for the shear-convection and neutral cases (Figures 17 and 18) show a general shape with a peak at small wavenumbers corresponding to the large-scale structures in the flow, and a tail that roughly follows $k^{-5/3}$ at intermediate wavenumbers, corresponding to the inertial subrange (Pope, 2000), and then drops below the $-5/3$ line at large wavenumbers due to dissipation.

For LES, the filter scale, which in our case is equivalent to the grid spacing, should be in the inertial subrange (e.g., Pope, 2000), where the expected slope of the spectrum is $-5/3$. Figure 17a shows that for the shear-convection case the horizontal velocity spectrum clearly follows the $-5/3$ line at various heights in the boundary layer in the 512^3 simulation, while the 128^3 simulation barely shows any inertial subrange. This resolution is on the limit of what is reasonable to use for LES; tests with lower resolutions clearly show erroneous behavior in some profiles. The 256^3 simulation with the TKE model resolves some of the inertial subrange, particularly away from the surface.

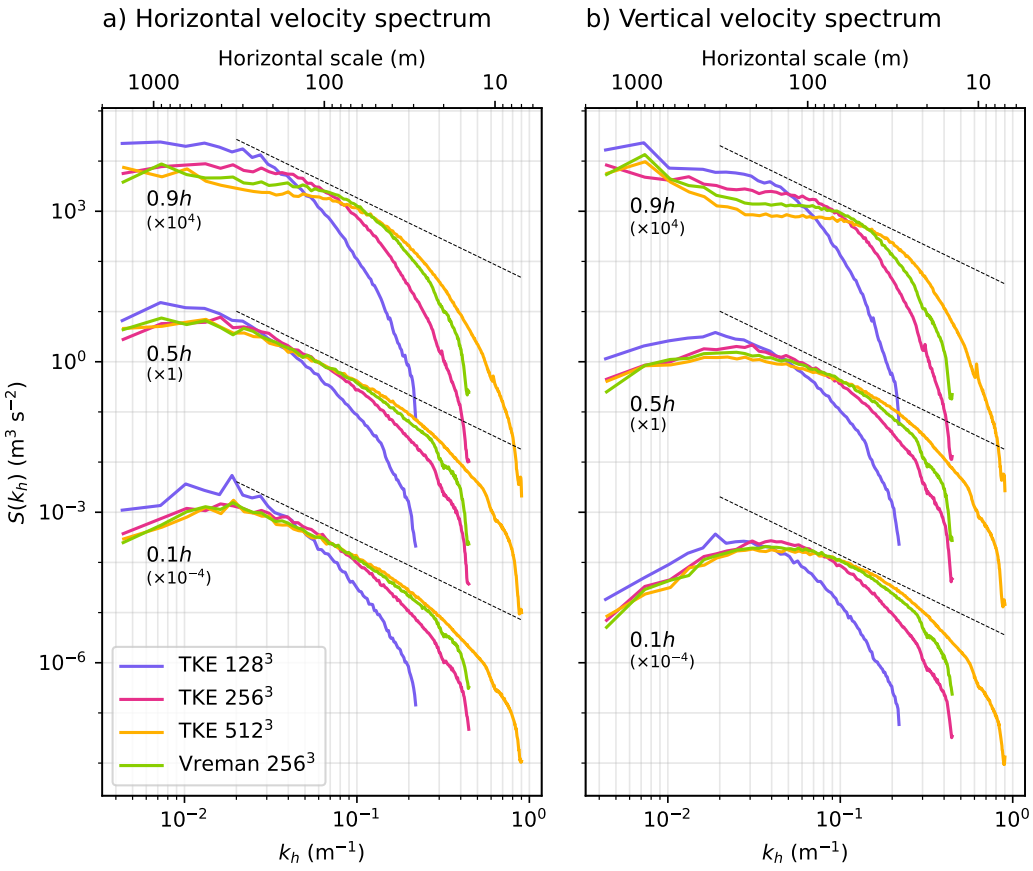

Figure 18. As Figure 17 but for the neutral case.

The spectra from the 256^3 simulation with the Vreman model are remarkably close to the 512^3 TKE model spectra over a large range of wavenumbers. This is in line with the results discussed in section 5.1 where the Vreman model has been found to be substantially less dissipative and thus to retain finer scales in the flow (Figure 5). Figure 17 by itself could suggest that the Vreman model is superior, since at a given grid spacing it resolves finer scales than the TKE model, but as discussed throughout the results the smaller dissipation also has downsides.

The vertical velocity spectra (Figure 17b) show a broad peak which shifts to larger wavenumbers close to the surface, in line with results of Sullivan and Patton (2011). Similarly to the horizontal wind spectra, the inertial subrange is clear, visible and indicated in the 512^3, 256^3 and 128^3 simulations, respectively.

In the neutral case the behavior is similar (Figure 18). However, in that case the 128^3 simulation stands out from the other simulations for small wavenumbers at all heights, indicating that such a coarse resolution does affect the solution substantially, even in the largest scales. Close to the boundary layer top, where the turbulence is influenced by the presence of the capping inversion, the spectra are resolution-dependent at small wavenumbers. It should be noted that the data from which the spectra have been calculated were sampled at a few selected levels only, the heights of which were selected before the start of the simulation. Thus, the spectrum at $0.9h$ is not exactly at 90% of the actual boundary layer height; this may affect the results. In the shear-convection case this does not have an impact since h is very similar in all simulations.

5.5.2 Heat Conservation

Since SEM does not ensure continuity across the element boundaries in the gradients of the solution, it conserves heat only asymptotically. To verify that this works sufficiently well we follow Svensson et al. (2011) and compare the integrated heat content in the domain to the heat added to the domain at the surface boundary. Starting from

$$\frac{\partial \overline{\theta}}{\partial t} = -\frac{\partial \overline{w'\theta'}}{\partial z} \tag{18}$$

we integrate from the surface to the top of the domain and over some time span from $t = 0$ to t:

$$\int_0^t \int_0^{L_z} \frac{\partial \overline{\theta}}{\partial t} dz dt = -\int_0^t \int_0^{L_z} \frac{\partial \overline{w'\theta'}}{\partial z} dz dt. \tag{19}$$

Since $\overline{w'\theta'} = 0$ at $z = L_z$ we get

$$\Theta(t) - \Theta(0) \equiv \int_0^{L_z} \overline{\theta}(t) dz - \int_0^{L_z} \overline{\theta}(0) dz = -\int_0^t \overline{w'\theta'}(z = 0) dt. \tag{20}$$

We consider the neutral and shear-convection cases, where $\overline{w'\theta'}(z = 0) = Q_*$ is constant, such that the right-hand side is simply $Q_* t$. Figure 19 shows the result for the neutral and shear-convection cases, formulated as an error. In the neutral case $Q_* = 0$, so we define the error as

$$\text{Error} = \left[\frac{\Theta(t) - \Theta(0)}{\Theta(0)} - 1 \right] \times 100\%.$$

In the shear-convection case the error is instead

$$\text{Error} = \left[\frac{\Theta(t) - \Theta(0)}{Q_* t} - 1 \right] \times 100\%.$$

Figure 19a shows that in the neutral case the error is virtually zero for all resolutions and both SGS models; deviations from zero are on the order of the tolerance set in the

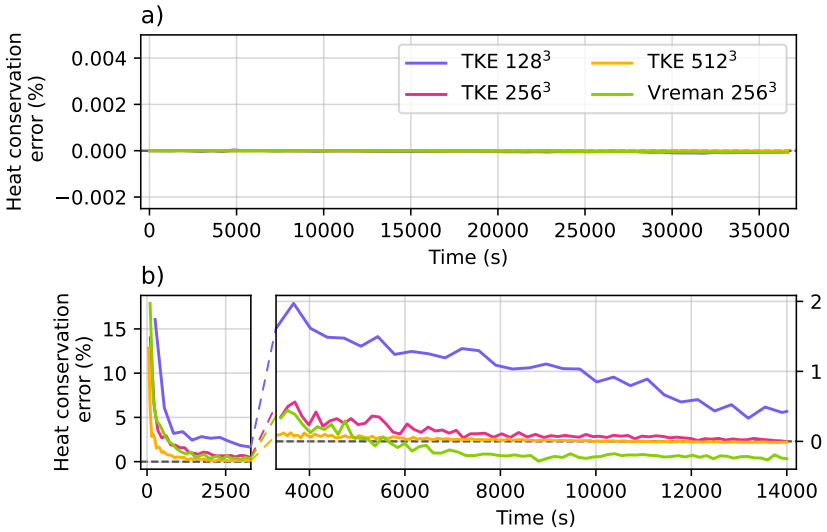

Figure 19. Error in the heat conservation in Nek5000 simulations of the a) neutral, and b) shear-convection cases at three different resolutions with the TKE model and 256^3 resolution with the Vreman model. The right part of panel b is zoomed in to better show the magnitude as it becomes smaller after the initial transient; the y-axis in the right part of the panel shows the same quantity as in the left part.

solver. In the shear-convection case (Figure 19b) there are substantial errors at the beginning of each simulation which quickly diminish after the initial period during which turbulence is spun up in the domain. After the initial transient, the error is resolution-dependent and very close to zero in the simulations with the TKE model at 256^3 and 512^3 resolution. It is noteworthy that the Vreman model seems to stabilize in a state where the amount of heat in the domain is somewhat smaller than what has been added through the surface boundary.

As the neutral case, where there is no surface heat flux, show essentially no error, we conclude that the errors that are present in the shear-convection case are due to the formulation of the surface boundary condition, and further investigation of this falls outside the scope of the current paper. The results show, however, that at sufficient resolution the errors are negligible.

6 Summary and Conclusions

We present a new large eddy simulation (LES) framework, using the turbulence solver Nek5000, for simulating turbulence in the atmospheric boundary layer (ABL) using the spectral element method (SEM). We simulate four canonical flow cases (neutral, free convection, shear-convection, and stably stratified boundary layers) and show that Nek5000 accurately captures the statistics and key flow features in all the cases.

Comparison of turbulence statistics with results from the established NCAR LES code shows good agreement for both first and higher order statistics. The Nek5000 solver is capable of capturing characteristic elements of each boundary layer type, such as the capping inversion in the neutral, free convection and shear-convection cases, the low-level jet in the neutral and stably stratified cases, and the large-scale coherent structures in all cases (shown for the neutral and stably stratified cases). Some differences are found in the temperature of the mixed layer, but overall the discrepancies between the two solvers

are of similar magnitude to differences between results from two Nek5000 simulations with different SGS models.

Profiles of first and second order statistics converge as well as expected for the range of presented resolutions, and turbulence spectra indicate that part of the inertial subrange is resolved in simulations with 256^3 and 512^3 computation points for the neutral and shear-convection cases.

Large eddy simulation of the atmospheric boundary layer involves simulating turbulence generated by both shear and buoyancy effects, as well as turbulence that is dampened by temperature stratification. SEM does not constrain gradients across element boundaries, which could potentially cause issues in this type of flow situations. For example, a non-smooth vertical temperature profile could cause erroneous vertical acceleration as the Boussinesq approximation is applied. The effect of the discontinuities can be moderated by the action of the SGS model. We have compared two different SGS models; one model based on Vreman (2004) and the Deardorff (1980) model based on the subgrid-scale TKE, and Figure B2b shows that the TKE model does a better job than the Vreman model at smoothing out irregularities at element boundaries and may thus be better suited for use with SEM.

However, while the TKE model does smooth the second order statistics somewhat at the element boundaries, there are still some discontinuities that may cause issues. Preliminary work on passive scalar advection indicates issues with conservation. There are methods for smoothing the solution, such as the gradient jump penalty stabilization designed to minimize numerical instabilities due to discontinuities in gradients at element boundaries (Moura et al., 2022); it could be investigated whether such an approach may also aid the solution in simulations of turbulence with buoyancy effects. It is, however, anticipated that any issues with scalar conservation will be reduced with increasing resolution. Performing simulations at high resolutions rather than designing tools to mitigate the issues related to an insufficient resolution is generally a preferable route as it limits uncertainties and biases introduced through model and parameter choices.

This paper documents that Nek5000, using SEM, is capable of simulating canonical ABL cases. Key features of the studied cases are well represented in the simulations, and the statistics align very well with results from the established NCAR LES solver. Going forward, our goal is to leverage the scalability of SEM and the currently available computational power to simulate atmospheric flows at high resolution, focusing on transient cases and the diurnal cycle and also working toward including cloud processes. It is with this in mind that we have chosen to work with SEM: it is not necessarily the best choice for the comparatively small cases presented in the present study but it has the capacity to solve very large problems efficiently. As Nek5000 runs only on CPUs, there is currently work ongoing to develop a new version of Nek5000: Neko (`https://neko.cfd/`; Jansson et al., 2024). Neko uses the same discretization methods as Nek5000 but is written in modern Fortran and designed to run on either CPUs or GPUs. Neko is currently undergoing tests with the here presented canonical cases, tests that a credible code for atmospheric boundary layer turbulence needs to pass. We will specifically examine the aspects that are critical for each of the flow types, to assure that the experimental configuration is adequate, i.e., a documented "recipe" for atmospheric LES experimentation.

7 Open Research

The Nek5000 source code used in this study is available at `https://github.com/Nek5000/Nek5000/commit/9b3d9227b5896dfef4bc5245d85c25f7ba12334d`. Furthermore, we have used utilities from the KTH Framework: `https://github.com/KTH-Nek5000/KTH_Framework/commit/810060c9cb6b23f2f5aa7754c09785aacf21266a` (Massaro et

al., 2024), as well as wall models implemented in NEKWMLES: `https://github.com/timofeymukha/nekwmles/commit/4987f5447f6aba4670cc87612137ee428538f992`.

The data underlying all figures in this paper is published at `https://bolin.su.se/data/huusko-2025-les-nek5000-1.1` (Huusko et al., 2025), and the Python scripts used to create the figures from the data are available at `https://git.bolin.su.se/bolin/huusko-2025-les-nek5000-1.1.0` (Huusko, 2025).

Acknowledgments

This work is supported by the Swedish e-Science Research Centre. The computations and data handling were enabled by resources provided by the National Academic Infrastructure for Supercomputing in Sweden (NAISS), partially funded by the Swedish Research Council through grant agreement no. 2022-06725. PPS was supported by NSF NCAR. We thank Ashwin Mohanan and Geert Brethouwer for their work laying the foundation for this study of the ABL with Nek5000. We also thank three anonymous reviewers for their thoughtful comments which helped improve the quality of this paper.

Appendix A TKE model in Nek5000

The TKE model (Deardorff, 1980) is based on integration of a prognostic equation for the subgrid-scale TKE (e):

$$\frac{\partial e}{\partial t} + \tilde{u}_j \frac{\partial e}{\partial x_j} = -\frac{\partial(\widetilde{u_j'' e} + \widetilde{u_j'' p''})}{\partial x_j} - \widetilde{u_i'' u_j''} \frac{\partial \tilde{u}_i}{\partial x_j} + \frac{g}{\theta_0} \widetilde{w'' \theta''} - \varepsilon, \tag{A1}$$

where the first term on the right-hand side represents turbulent transport of turbulence and pressure, the second term represents local shear production, the third term represents local buoyancy production, and the last term is dissipation.

Equation (A1) is integrated and the resulting e is used to calculate the eddy viscosity and diffusivity at each point in space as

$$K_m = c_K l \sqrt{e}, \tag{A2}$$

$$K_h = \left(1 + 2\frac{l}{\Delta}\right) K_m, \tag{A3}$$

where c_K is a constant, here assigned the value $c_K = 0.1$ (Deardorff, 1980), l is a length scale, and Δ is the grid spacing, here taken to be the maximum grid spacing $\Delta^{\max} = \max(\Delta_{x,y}^{\max}, \Delta_z^{\max})$, see Table 1. For the length scale l we use

$$l = \min\left[0.76\sqrt{\frac{e}{N_\theta^2}}; \Delta\right] \tag{A4}$$

where $N_\theta = \sqrt{(g/\theta_0)/(\partial\theta/\partial z)}$ is the Brunt-Väisälä frequency.

The terms on the right-hand side of equation (A1) involves subgrid-scale variables which require modeling. Following Deardorff (1980), we let

$$\widetilde{u_j'' e} + \widetilde{u_j'' p''} = -2K_m \frac{\partial e}{\partial x_j}, \tag{A5}$$

$$\widetilde{u_i'' u_j''} = -K_m \left(\frac{\partial \tilde{u}_i}{\partial x_j} + \frac{\partial \tilde{u}_j}{\partial x_i}\right) = -2K_m \tilde{S}_{ij}, \tag{A6}$$

and

$$\widetilde{w'' \theta''} = -K_h \frac{\partial \tilde{\theta}}{\partial z}. \tag{A7}$$

Furthermore, we parameterize the molecular dissipation as

$$\varepsilon = \frac{c_0 e^{3/2}}{l}, \tag{A8}$$

where $c_0 \sim 0.19 + 0.74l/\Delta$ (Moeng & Sullivan, 2015). To summarise, the equation to be integrated, expressed in only filtered variables, is

$$\frac{\partial e}{\partial t} + \frac{\partial \tilde{u}_j e}{\partial x_j} = \frac{\partial}{\partial x_j}\left(2K_m \frac{\partial e}{\partial x_j}\right) + 2K_m \tilde{S}_{ij}\frac{\partial \tilde{u}_i}{\partial x_j} - \frac{g}{\theta_0}K_h\frac{\partial \tilde{\theta}}{\partial z} - \frac{c_0 e^{3/2}}{l}, \tag{A9}$$

and the value for e at each point in space and time is used to calculate the eddy viscosity and diffusivity (equations A2 and A3).

Appendix B Vreman model in Nek5000

The Vreman model (Vreman, 2004) implemented in Nek5000 uses an eddy viscosity of the form

$$K_m = C\sqrt{\left(\frac{B_\beta}{\alpha_{ij}\alpha_{ij}}\right)}, \tag{B1}$$

with $\alpha_{ij} = \partial\tilde{u}_i/\partial x_j$ and $B_\beta = \beta_{11}\beta_{22} - \beta_{12}^2 + \beta_{11}\beta_{33} - \beta_{13}^2 + \beta_{22}\beta_{33} - \beta_{23}^2$, where $\beta_{ij} = \Delta^2\alpha_{mi}\alpha_{mj}$ (summed over $m = 1, 2, 3$). The filter witdh Δ is taken here to be the maximum grid spacing $\Delta^{\max} = \max(\Delta_{x,y}^{\max}, \Delta_z^{\max})$ (see Table 1). The constant C is related to the Smagorinsky constant as $C \approx 2.5C_S^2$ (Vreman, 2004); we use $C_S = 0.16$, and thus $C = 0.064$, in all simulations. The Vreman model is designed to maintain the simplicity of the Smagorinsky-Lilly model but with less dissipation in near-wall and transitional regions. It has been used for LES of the ABL by Fuka and Brechler (2011) (using a solver based on the method of lines) and Van Hooft et al. (2019) (using a finite volume method solver), neither of whom evaluate the performance of the model in any detail.

When we use the Vreman model, the subgrid-scale heat flux is modeled using a prescribed subgrid-scale Prandtl number which varies depending on the stratification:

$$K_h = \frac{K_m}{\mathrm{Pr}}. \tag{B2}$$

The subgrid-scale Prandtl number is here set to 1 for the stably stratified boundary layer simulation, and 1/3 for all other cases, to emulate how the eddy diffusivity in the TKE model (equation (A3)) behaves in different stability regimes (under convective conditions, $l \sim \Delta$, while for a stable boundary layer l is smaller, corresponding to a larger N_θ in equation (A4), meaning that $K_h \sim K_m$). This prescription of a constant subgrid-scale Prandtl number in the entire domain is not an ideal solution as the stratification varies substantially with height, particularly across the inversion layer, in an ABL.

Initial test simulations showed that the Vreman model in its original formulation (equation B1), which includes no information about the temperature structure of the atmosphere, tends to give a less sharp temperature inversion than what is found in the reference simulations. To include the effect of the temperature stratification on the subgrid-scale fluxes we apply a stability correction using the Richardson number, as described by Moeng and Sullivan (2015). Applying the correction to the eddy viscosity of the Vreman model gives us

$$K_m^{\mathrm{corr}} = \left(1 - \frac{\mathrm{Ri}}{\mathrm{Ri}_c}\right)^{1/2} K_m, \tag{B3}$$

where Ri is the Richardson number, calculated as

$$\mathrm{Ri} = \frac{\frac{g}{\theta_0}\frac{\partial\theta}{\partial z}}{\left(\frac{\partial u}{\partial z}\right)^2 + \left(\frac{\partial v}{\partial z}\right)^2}, \tag{B4}$$

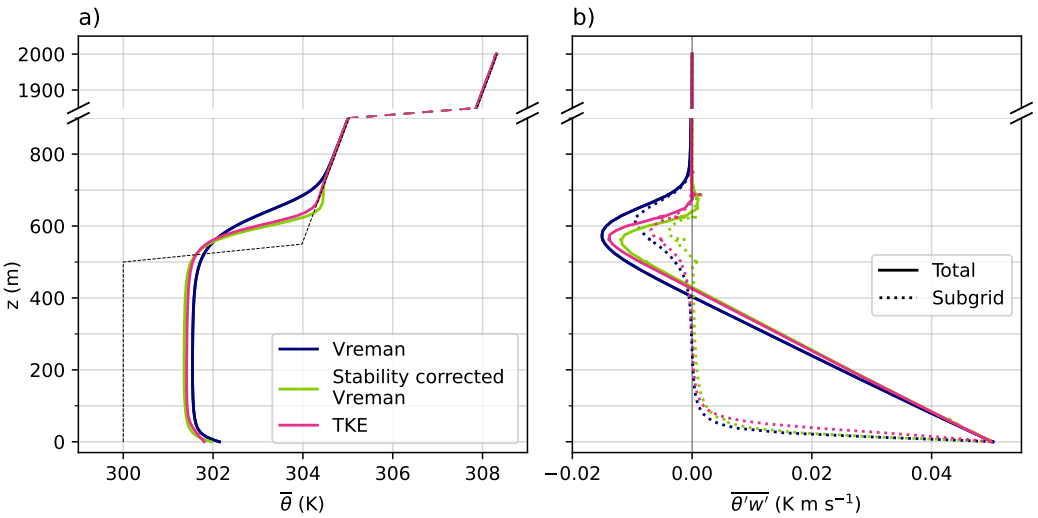

Figure B1. Comparison of three different SGS models (Vreman, equation (B1); stability corrected Vreman, equation (B3); and TKE, equation (A2)) in Nek5000, and reference data from the NCAR LES for mean profiles of a) temperature, and b) vertical heat flux (subgrid and total), in the shear-convection case.

and Ri_c is the critical Richardson number, here set to 0.25 (Stull, 1988). The eddy diffusivity is then calculated according to equation (B2). If $\mathrm{Ri}>\mathrm{Ri}_c$, we set $K_m = 10^{-10}$.

The stability correction gives a sharper temperature inversion and a smaller entrainment of heat in the shear-convection case, leading to a somewhat cooler mixed layer. This brings the profiles to closer agreement with the reference data as well as with Nek5000 simulations using the TKE model (Figure B1), although as mentioned in section 5.3 it also introduces an overshoot in both temperature and heat flux just above the inversion.

The influence on the velocity is not as large (Figure B2a), and both versions of the Vreman model give a smaller mixed-layer $\overline{u}$ than the reference. Figure B2b shows that the stability correction emphasizes the influence of the element boundaries on the eddy viscosity. It should, however, be emphasized that this behavior has its root in the mathematical properties of SEM and is not caused by any version of the Vreman model; we simply observe in our results that the TKE model seems to mitigate the discontinuities while the stability corrected Vreman model magnifies them.

In the neutral case the influence of the stability correction is small and there is good agreement between all three SGS models (Vreman, stability corrected Vreman, and TKE). Figures equivalent to Figures B1 and B2 are therefore not shown for the neutral case.

Appendix C Sponge Layer

The damping layer in Nek5000 consists of a region at the top of the domain where a forcing is applied (added to the right hand side of equation (1)) to dampen the strength of velocity variations (Chevalier et al., 2007). The forcing is formulated as

$$F_i = \lambda(z)(U_i - u_i), \tag{C1}$$

where U_i is a specified constant velocity (given as the geostrophic velocity in our simulations) and λ is is a sponge function given by

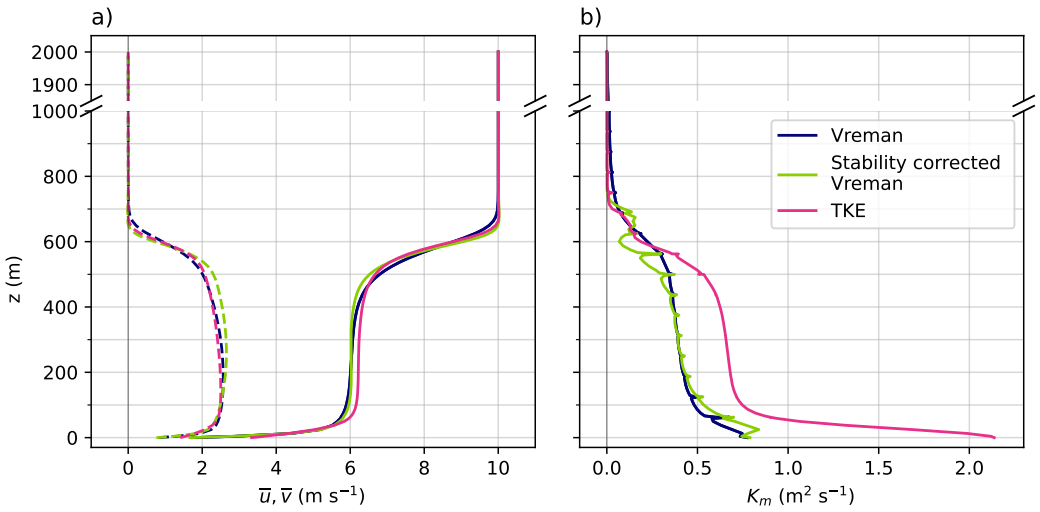

Figure B2. As Figure B1 but for a) horizontal velocities ($\overline{u}$ in full lines, $\overline{v}$ in dashed lines,) and b) subgrid-scale eddy viscosity (not available from the NCAR LES).

Table C1. Parameter values used in the sponge layer for the different cases.

Case	λ_{max} (s^{-1})	Δ_w (m)	Δ_d (m)
Neutral	0.01	200	150
Free convection	0.01	200	150
Shear-convection	0.01	200	150
Stably stratified	0.01	50	30

$$\lambda(z) = \lambda_{max}\sigma((z - L_z + \Delta_w)/\Delta_d). \tag{C2}$$

Here, λ_{max} is a parameter that gives the maximum amplitude of the damping layer. The layer occupies a region of width Δ_w (as given for each case in Table 1), extending down from the top of the domain. The parameter Δ_d defines the width of the drop of the sponge. The step function σ is defined as

$$\sigma(x) = \begin{cases} 0 & \text{if } x \leq 0.001, \\ (1 + \exp((x-1)^{-1} + x^{-1}))^{-1} & \text{if } 0.001 < x \leq 0.999, \\ 1 & \text{if } x > 0.999. \end{cases} \tag{C3}$$

The values for the damping layer parameters are given in Table C1.

Appendix D Computation of Energy Spectral Density

To compute two-dimensional energy spectra of a variable a we use a Fast Fourier Transform (FFT) algorithm to compute the discrete Fourier Transform according to

$$F(k_x, k_y) = \sum_{n=0}^{N-1}\sum_{m=0}^{M-1} \frac{a_{nm}}{NM} \exp(-i2\pi nk_n/N - i2\pi mk_m/M), \tag{D1}$$

where M, N are the number of sampling points in the x and y directions, respectively, and $k_x = \frac{2\pi}{\Delta x}$ and $k_y = \frac{2\pi}{\Delta y}$ are the wavenumbers in the x and y directions, respectively. Following Stull (1988) we then compute the discrete spectral energy, $E(k_x, k_y)$, as

$$E(k_x, k_y) = |F(k_x, k_y)|^2, \tag{D2}$$

and the energy spectral density, $S(k_x, k_y)$, as

$$S(k_x, k_y) = \frac{E(k_x, k_y)}{\Delta k_x \Delta k_y}. \tag{D3}$$

This procedure results in a energy spectral density that when integrated over the wavenumbers in both directions yields the total variance of the original velocity field. For easier interpretation of the result, this two-dimensional energy spectral density is projected onto the total horizontal wavenumber $k_h = \sqrt{k_x^2 + k_y^2}$ by integrating

$$S(k_h) = \int_0^{2\pi} S(k_x, k_y) k_h d\theta, \tag{D4}$$

where $k_x = k_h \cos\theta$ and $k_x = k_h \sin\theta$, to yield the line plots in Figures 17 and 18 (e.g., Wyngaard, 2010).

In Figures 17 and 18 this procedure is applied on the horizontal and vertical wind speed, respectively, over a horizontal plane at different heights. The resulting energy spectral density, or "spectrum", is then smoothed by averaging over circular bins (the data is binned into given ranges of k_h and an average is computed over each bin) as well as averaged over the time intervals indicated for each case in Table 1.

The discrete Fourier transform requires data on an equidistantly spaced grid, which we do not have in our solution since the SEM solution is computed on non-equidistant GLL points. We therefore interpolate the solution to an equidistant grid before computing the spectra. For the grid spacing we choose the maximum spacing between the GLL points, as that is the smallest scale that is resolved everywhere in the domain. The number of bins for the radial averaging is chosen as the number of sampling points in each direction.

References

Angevine, W. M., Edwards, J. M., Lothon, M., LeMone, M. A., & Osborne, S. R. (2020). Transition Periods in the Diurnally-Varying Atmospheric Boundary Layer Over Land. *Boundary-Layer Meteorology*, *177*(2-3), 205–223. doi: 10.1007/s10546-020-00515-y

Beare, R. J. (2008). The Role of Shear in the Morning Transition Boundary Layer. *Boundary-Layer Meteorology*, *129*(3), 395–410. doi: 10.1007/s10546-008-9324-8

Beare, R. J., Macvean, M. K., Holtslag, A. A. M., Cuxart, J., Esau, I., Golaz, J.-C., ... Sullivan, P. (2006). An Intercomparison of Large-Eddy Simulations of the Stable Boundary Layer. *Boundary-Layer Meteorology*, *118*(2), 247–272. doi: 10.1007/s10546-004-2820-6

Berg, J., Patton, E. G., & Sullivan, P. P. (2020). Large-Eddy Simulation of Conditionally Neutral Boundary Layers: A Mesh Resolution Sensitivity Study. *Journal of the Atmospheric Sciences*, *77*(6), 1969–1991. doi: 10.1175/JAS-D-19-0252.1

Bou-Zeid, E. (2015). Challenging the Large Eddy Simulation Technique with Advanced *a posteriori* Tests. *Journal of Fluid Mechanics*, *764*, 1–4. doi: 10.1017/jfm.2014.616

Brasseur, J. G., & Wei, T. (2010). Designing large-eddy simulation of the turbulent boundary layer to capture law-of-the-wall scaling. *Physics of Fluids*, *22*(2), 021303. doi: 10.1063/1.3319073

Chatterjee, T., & Peet, Y. (2015). Actuator Line Wind Turbine Simulations in Atmospheric Turbulent Flows using Spectral Element Method. In *33rd Wind Energy Symposium.* Kissimmee, Florida: American Institute of Aeronautics and Astronautics. doi: 10.2514/6.2015-0727

Chatterjee, T., & Peet, Y. T. (2017). Effect of Artificial Length Scales in Large Eddy Simulation of a Neutral Atmospheric Boundary Layer Flow: A Simple Solution to Log-Layer Mismatch. *Physics of Fluids*, *29*(7), 075105. doi: 10.1063/1.4994603

Chevalier, M., Schlatter, P., Lundbladh, A., & Henningson, D. (2007). *SIMSON: A Pseudo-Spectral Solver for Incompressible Boundary Layer Flows.* Mekanik, Kungliga Tekniska Högskolan.

Deardorff, J. W. (1970). A Numerical Study of Three-Dimensional Turbulent Channel Flow at Large Reynolds Numbers. *Journal of Fluid Mechanics*, *41*(2), 453–480. doi: 10.1017/S0022112070000691

Deardorff, J. W. (1971). On the Magnitude of the Subgrid Scale Eddy Coefficient. *Journal of Computational Physics*, *7*(1), 120–133. doi: 10.1016/0021-9991(71)90053-2

Deardorff, J. W. (1972). Numerical Investigation of Neutral and Unstable Planetary Boundary Layers. *Journal of the Atmospheric Sciences*, *29*(1), 91–115. doi: 10.1175/1520-0469(1972)029⟨0091:NIONAU⟩2.0.CO;2

Deardorff, J. W. (1980). Stratocumulus-Capped Mixed Layers Derived from a Three-Dimensional Model. *Boundary-Layer Meteorology*, *18*(4), 495–527. doi: 10.1007/BF00119502

Dennis, J. M., Edwards, J., Evans, K. J., Guba, O., Lauritzen, P. H., Mirin, A. A., ... Worley, P. H. (2012). CAM-SE: A Scalable Spectral Element Dynamical Core for the Community Atmosphere Model. *The International Journal of High Performance Computing Applications*, *26*(1), 74–89. doi: 10.1177/1094342011428142

Dyer, A. J. (1974). A Review of Flux-Profile Relationships. *Boundary-Layer Meteorology*, *7*(3), 363–372. doi: 10.1007/BF00240838

Edwards, J. M., Basu, S., Bosveld, F. C., & Holtslag, A. A. M. (2014). The Impact of Radiation on the GABLS3 Large-Eddy Simulation through the Night and during the Morning Transition. *Boundary-Layer Meteorology*, *152*(2), 189–211. doi: 10.1007/s10546-013-9895-x

El Khoury, G. K., Schlatter, P., Noorani, A., Fischer, P. F., Brethouwer, G., & Johansson, A. V. (2013). Direct Numerical Simulation of Turbulent Pipe Flow at Moderately High Reynolds Numbers. *Flow, Turbulence and Combustion*, *91*(3), 475–495. doi: 10.1007/s10494-013-9482-8

Fischer, P. (1997). An Overlapping Schwarz Method for Spectral Element Solution of the Incompressible Navier–Stokes Equations. *Journal of Computational Physics*, *133*(1), 84–101. doi: 10.1006/jcph.1997.5651

Fischer, P., Kerkemeier, S., Min, M., Lan, T.-H., Phillips, M., Rathnayake, T., ... Warburton, T. (2022). NekRS, a GPU-accelerated Spectral Element Navier–Stokes Solver. *Parallel Computing*. doi: 10.1016/j.parco.2022.102982

Fischer, P., Lottes, J. W., & Kerkemeier, S. G. (2008). *nek5000 Web page.* (http://nek5000.mcs.anl.gov)

Foken, T. (2006). 50 Years of the Monin–Obukhov Similarity Theory. *Boundary-Layer Meteorology*, *119*(3), 431–447. doi: 10.1007/s10546-006-9048-6

Fuka, V., & Brechler, J. (2011). Large Eddy Simulation of the Stable Boundary Layer. In J. Fořt, J. Fürst, J. Halama, R. Herbin, & F. Hubert (Eds.), *Finite Volumes for Complex Applications VI Problems & Perspectives* (Vol. 4, pp. 485–493). Berlin, Heidelberg: Springer Berlin Heidelberg. doi: 10.1007/978-3-642-20671-9_51

Germano, M., Piomelli, U., Moin, P., & Cabot, W. H. (1991). A Dynamic Subgrid-Scale Eddy Viscosity Model. *Physics of Fluids A: Fluid Dynamics*, *3*(7), 1760–

1765. doi: 10.1063/1.857955

Hu, X., Yang, X., & Ilhwan Park, G. (2024). On the Grid Convergence of Wall-Modeled Large-Eddy Simulation. *Journal of Computational Physics*, *504*, 112884. doi: 10.1016/j.jcp.2024.112884

Huusko, L. (2025). *Python scripts for analysing output from large eddy simulations of the atmospheric boundary layer with the fluid dynamics code nek5000.* Software version 1.1.0. Bolin Centre Code Repository. (Software) doi: 10.57669/huusko-2025-les-nek5000-1.1.0

Huusko, L., Mukha, T., Donati, L. L., Sullivan, P., Schlatter, P., & Svensson, G. (2025). *Large eddy simulation data of quasi-stationary atmospheric boundary layers with the fluid dynamics code nek5000.* Dataset version 1.1. Bolin Centre Database. (Dataset) doi: 10.17043/huusko-2025-les-nek5000-1.1

Jansson, N., Karp, M., Podobas, A., Markidis, S., & Schlatter, P. (2024). Neko: A Modern, Portable, and Scalable Framework for High-Fidelity Computational Fluid Dynamics. *Computers & Fluids*, *275*, 106243. doi: 10.1016/j.compfluid.2024.106243

Karniadakis, G. E., Israeli, M., & Orszag, S. A. (1991). High-Order Splitting Methods for the Incompressible Navier-Stokes Equations. *Journal of Computational Physics*, *97*(2), 414–443. doi: 10.1016/0021-9991(91)90007-8

Kawai, S., & Larsson, J. (2012). Wall-Modeling in Large Eddy Simulation: Length Scales, Grid Resolution, and Accuracy. *Physics of Fluids*, *24*(1), 015105. doi: 10.1063/1.3678331

Klemp, J. B., & Durran, D. R. (1983). An Upper Boundary Condition Permitting Internal Gravity Wave Radiation in Numerical Mesoscale Models. *Monthly Weather Review*, *111*(3), 430–444. doi: 10.1175/1520-0493(1983)111⟨0430:AUBCPI⟩2.0.CO;2

Lanzilao, L., & Meyers, J. (2023). An Improved Fringe-Region Technique for the Representation of Gravity Waves in Large Eddy Simulation with Application to Wind Farms. *Boundary-Layer Meteorology*, *186*(3), 567–593. doi: 10.1007/s10546-022-00772-z

Li, D. (2019). Turbulent Prandtl Number in the Atmospheric Boundary Layer - Where Are We Now? *Atmospheric Research*, *216*, 86–105. doi: 10.1016/j.atmosres.2018.09.015

Lilly, D.K. (1967). The Representation of Small-Scale Turbulence in Numerical Simulations. In *Proceedings IBM scientific computing symposium on environmental sciences* (pp. 195–209). Yorktown Heights, NY.

Maday, Y., & Patera, A. T. (1989). Spectral Element Methods for the Incompressible Navier-Stokes Equations. In A. K. Noor & J. T. Oden (Eds.), *State-of-the-art surveys on computational mechanics* (pp. 71–143). New York, American Society of Mechanical Engineers.

Malm, J., Schlatter, P., Fischer, P. F., & Henningson, D. S. (2013). Stabilization of the Spectral Element Method in Convection Dominated Flows by Recovery of Skew-Symmetry. *Journal of Scientific Computing*, *57*(2), 254–277. doi: 10.1007/s10915-013-9704-1

Maronga, B., Knigge, C., & Raasch, S. (2020). An Improved Surface Boundary Condition for Large-Eddy Simulations Based on Monin–Obukhov Similarity Theory: Evaluation and Consequences for Grid Convergence in Neutral and Stable Conditions. *Boundary-Layer Meteorology*, *174*(2), 297–325. doi: 10.1007/s10546-019-00485-w

Massaro, D., Peplinski, A., Stanly, R., Mirzareza, S., Lupi, V., Mukha, T., & Schlatter, P. (2024). A Comprehensive Framework to Enhance Numerical Simulations in the Spectral-Element Code Nek5000. *Computer Physics Communications*, *302*, 109249. doi: 10.1016/j.cpc.2024.109249

Matheou, G. (2016). Numerical Discretization and Subgrid-scale Model Effects on Large-eddy Simulations of a Stable Boundary Layer. *Quarterly Journal of the*

Royal Meteorological Society, *142*(701), 3050–3062. doi: 10.1002/qj.2888

McWilliams, J. C., Meneveau, C., Patton, E. G., & Sullivan, P. P. (2023). Stable Boundary Layers and Subfilter-Scale Motions. *Atmosphere*, *14*(7), 1107. doi: 10.3390/atmos14071107

McWilliams, J. C., & Restrepo, J. M. (1999). The Wave-Driven Ocean Circulation. *Journal of Physical Oceanography*, *29*(10), 2523–2540. doi: 10.1175/1520-0485(1999)029⟨2523:TWDOC⟩2.0.CO;2

Mirocha, J. D., & Kosović, B. (2010). A Large-Eddy Simulation Study of the Influence of Subsidence on the Stably Stratified Atmospheric Boundary Layer. *Boundary-Layer Meteorology*, *134*(1), 1. doi: 10.1007/s10546-009-9449-4

Mironov, D., & Sullivan, P. (2024). Turbulence Structure and Mixing in Strongly Stable Couette Flows over Thermally Heterogeneous Surfaces: Effect of Heterogeneity Orientation. *Flow, Turbulence and Combustion*, *114*(3), 967–994. doi: 10.1007/s10494-024-00593-9

Moeng, C.-H. (1984). A Large-Eddy-Simulation Model for the Study of Planetary Boundary-Layer Turbulence. *Journal of the Atmospheric Sciences*, *41*(13), 2052–2062. doi: 10.1175/1520-0469(1984)041⟨2052:ALESMF⟩2.0.CO;2

Moeng, C.-H., & Rotunno, R. (1990). Vertical-Velocity Skewness in the Buoyancy-Driven Boundary Layer. *Journal of the Atmospheric Sciences*, *47*(9), 1149–1162. doi: 10.1175/1520-0469(1990)047⟨1149:VVSITB⟩2.0.CO;2

Moeng, C.-H., & Sullivan, P. (2015). Numerical Models | Large-Eddy Simulation. In *Encyclopedia of Atmospheric Sciences* (pp. 232–240). Elsevier. doi: 10.1016/B978-0-12-382225-3.00201-2

Moeng, C.-H., & Wyngaard, J. C. (1988). Spectral Analysis of Large-Eddy Simulations of the Convective Boundary Layer. *Journal of the Atmospheric Sciences*, *45*(23), 3573–3587. doi: 10.1175/1520-0469(1988)045⟨3573:SAOLES⟩2.0.CO;2

Monin, A. S., & Obukhov, A. M. (1954). Basic Laws of Turbulent Mixing in the Surface Layer of the Atmosphere. *Tr Akad Nauk SSSR Geofiz Inst*, *24*(151), 163–187.

Moura, R. C., Cassinelli, A., Da Silva, A. F., Burman, E., & Sherwin, S. J. (2022). Gradient Jump Penalty Stabilisation of Spectral/ h p Element Discretisation for under-Resolved Turbulence Simulations. *Computer Methods in Applied Mechanics and Engineering*, *388*, 114200. doi: 10.1016/j.cma.2021.114200

Müller, A., Kopera, M. A., Marras, S., Wilcox, L. C., Isaac, T., & Giraldo, F. X. (2019). Strong Scaling for Numerical Weather Prediction at Petascale with the Atmospheric Model NUMA. *The International Journal of High Performance Computing Applications*, *33*(2), 411–426. doi: 10.1177/1094342018763966

Offermans, N., Marin, O., Schanen, M., Gong, J., Fischer, P., Schlatter, P., ... Merzari, E. (2016). On the Strong Scaling of the Spectral Element Solver Nek5000 on Petascale Systems. In *Proceedings of the Exascale Applications and Software Conference 2016* (pp. 1–10). doi: 10.1145/2938615.2938617

Offermans, N., Peplinski, A., Marin, O., & Schlatter, P. (2020). Adaptive Mesh Refinement For Steady Flows in Nek5000. *Computers & Fluids*, *197*, 104352. doi: 10.1016/j.compfluid.2019.104352

Patera, A. T. (1984). A Spectral Element Method for Fluid Dynamics: Laminar Flow in a Channel Expansion. *Journal of Computational Physics*, *54*(3), 468–488. doi: 10.1016/0021-9991(84)90128-1

Pope, S. B. (2000). *Turbulent flows*. Cambridge ; New York: Cambridge University Press.

Scheel, J. D., Emran, M. S., & Schumacher, J. (2013). Resolving the Fine-Scale Structure in Turbulent Rayleigh–Bénard Convection. *New Journal of Physics*, *15*(11), 113063. doi: 10.1088/1367-2630/15/11/113063

Schmidt, H., & Schumann, U. (1989). Coherent Structure of the Convective Boundary Layer Derived from Large-Eddy Simulations. *Journal of Fluid Mechanics*, *200*, 511–562. doi: 10.1017/S0022112089000753

Smagorinsky, J. (1963). General Circulation Experiments with the Primitive Equations: I. The Basic Experiment*. *Monthly Weather Review*, *91*(3), 99–164. doi: 10.1175/1520-0493(1963)091⟨0099:GCEWTP⟩2.3.CO;2

Spalart, P. R., Moser, R. D., & Rogers, M. M. (1991). Spectral Methods for the Navier-Stokes Equations with One Infinite and Two Periodic Directions. *Journal of Computational Physics*, *96*(2), 297–324. doi: 10.1016/0021-9991(91)90238-G

Stiperski, I., & Calaf, M. (2023). Generalizing Monin-Obukhov Similarity Theory (1954) for Complex Atmospheric Turbulence. *Physical Review Letters*, *130*(12), 124001. doi: 10.1103/PhysRevLett.130.124001

Stoll, R., Gibbs, J. A., Salesky, S. T., Anderson, W., & Calaf, M. (2020). Large-Eddy Simulation of the Atmospheric Boundary Layer. *Boundary-Layer Meteorology*, *177*(2-3), 541–581. doi: 10.1007/s10546-020-00556-3

Stull, R. B. (Ed.). (1988). *An Introduction to Boundary Layer Meteorology*. Dordrecht: Springer Netherlands. doi: 10.1007/978-94-009-3027-8

Sullivan, P. P., Edson, J. B., Hristov, T., & McWilliams, J. C. (2008). Large-Eddy Simulations and Observations of Atmospheric Marine Boundary Layers above Nonequilibrium Surface Waves. *Journal of the Atmospheric Sciences*, *65*(4), 1225–1245. doi: 10.1175/2007JAS2427.1

Sullivan, P. P., & McWilliams, J. C. (2010). Dynamics of Winds and Currents Coupled to Surface Waves. *Annual Review of Fluid Mechanics*, *42*(1), 19–42. doi: 10.1146/annurev-fluid-121108-145541

Sullivan, P. P., McWilliams, J. C., & Moeng, C.-H. (1994). A Subgrid-Scale Model for Large-Eddy Simulation of Planetary Boundary-Layer Flows. *Boundary-Layer Meteorology*, *71*(3), 247–276. doi: 10.1007/BF00713741

Sullivan, P. P., McWilliams, J. C., & Moeng, C.-H. (1996). A Grid Nesting Method for Large-Eddy Simulation of Planetary Boundary-Layer Flows. *Boundary-Layer Meteorology*, *80*(1-2), 167–202. doi: 10.1007/BF00119016

Sullivan, P. P., & Patton, E. G. (2011). The Effect of Mesh Resolution on Convective Boundary Layer Statistics and Structures Generated by Large-Eddy Simulation. *Journal of the Atmospheric Sciences*, *68*(10), 2395–2415. doi: 10.1175/JAS-D-10-05010.1

Sullivan, P. P., Weil, J. C., Patton, E. G., Jonker, H. J. J., & Mironov, D. V. (2016). Turbulent Winds and Temperature Fronts in Large-Eddy Simulations of the Stable Atmospheric Boundary Layer. *Journal of the Atmospheric Sciences*, *73*(4), 1815–1840. doi: 10.1175/JAS-D-15-0339.1

Svensson, G., & Holtslag, A. A. M. (2009). Analysis of Model Results for the Turning of the Wind and Related Momentum Fluxes in the Stable Boundary Layer. *Boundary-Layer Meteorology*, *132*(2), 261–277. doi: 10.1007/s10546-009-9395-1

Svensson, G., Holtslag, A. A. M., Kumar, V., Mauritsen, T., Steeneveld, G. J., Angevine, W. M., ... Zampieri, M. (2011). Evaluation of the Diurnal Cycle in the Atmospheric Boundary Layer Over Land as Represented by a Variety of Single-Column Models: The Second GABLS Experiment. *Boundary-Layer Meteorology*, *140*(2), 177–206. doi: 10.1007/s10546-011-9611-7

Tombouldies, A., Min, M., Fischer, P., Churchfield, M., & Sprague, M. (2023). *Advanced Turbulence Models for Large-Scale Atmospheric Boundary Layer Flows* (Tech. Rep.). United States. doi: 10.2172/2229259

Tomboulides, A., Churchfield, M., Fischer, P., Sprague, M., & Min, M. (2024). *Modeling Turbulence in the Atmospheric Boundary Layer with Spectral Element and Finite Volume Methods* (No. arXiv:2410.00147). arXiv.

Tufo, H., & Fischer, P. (2001). Fast Parallel Direct Solvers for Coarse Grid Problems. *Journal of Parallel and Distributed Computing*, *61*(2), 151–177. doi: 10.1006/jpdc.2000.1676

Van Hooft, J. A., Baas, P., Van Tiggelen, M., Ansorge, C., & Van De Wiel, B. J. H.

(2019). An Idealized Description for the Diurnal Cycle of the Dry Atmospheric Boundary Layer. *Journal of the Atmospheric Sciences*, *76*(12), 3717–3736. doi: 10.1175/JAS-D-19-0023.1

Vreman, A. W. (2004). An Eddy-Viscosity Subgrid-Scale Model for Turbulent Shear Flow: Algebraic Theory and Applications. *Physics of Fluids*, *16*(10), 3670–3681. doi: 10.1063/1.1785131

Wyngaard, J. C. (2010). *Turbulence in the Atmosphere* (1st ed.). Cambridge University Press. doi: 10.1017/CBO9780511840524

Zaron, E. D., Chua, B. S., Reinecke, P. A., Michalakes, J., Doyle, J. D., & Xu, L. (2022). The Tangent-Linear and Adjoint Models of the NEPTUNE Dynamical Core. *Tellus A: Dynamic Meteorology and Oceanography*. doi: 10.16993/tellusa.146

Figure1.

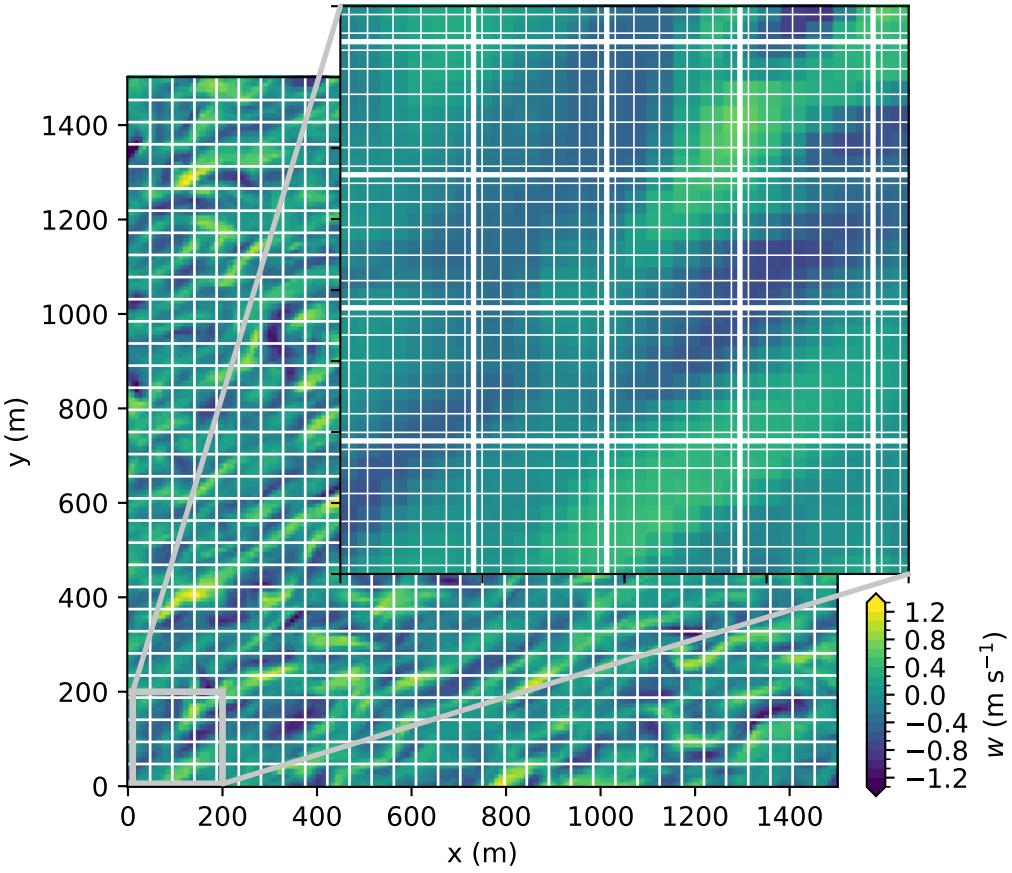
y (m)
0
200
400
600
800
1000
1200
1400
x (m)
0
200
400
600
800
1000
1200
1400
w (m s−1)
1.2
0.8
0.4
0.0
−0.4
−0.8
−1.2

Figure2.

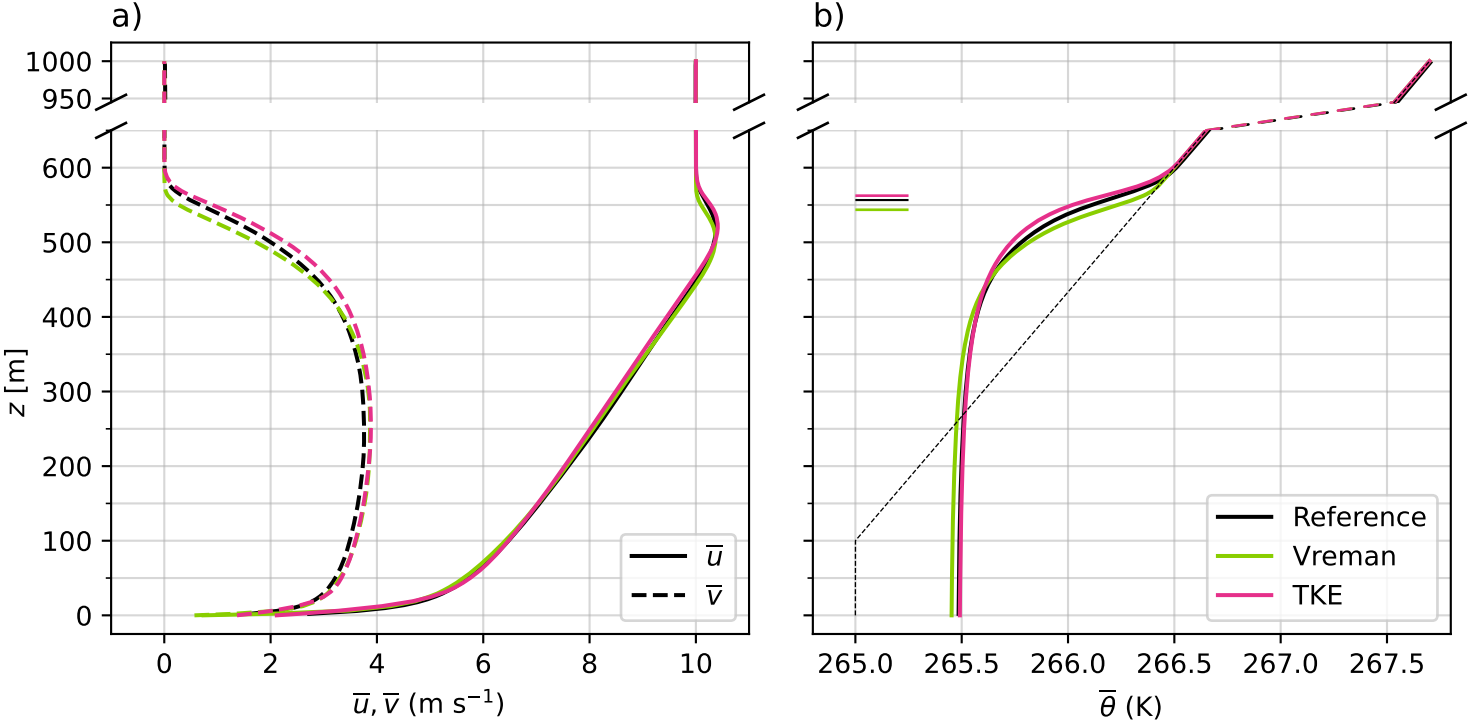
a)
b)
1000
950
600
500
400
300
200
100
0
z [m]
0
2
4
6
8
10
$\overline{u}, \overline{v}$ (m s^{-1})
$\overline{u}$
$\overline{v}$
265.0
265.5
266.0
266.5
267.0
267.5
$\overline{\theta}$ (K)
Reference
Vreman
TKE

Figure3.

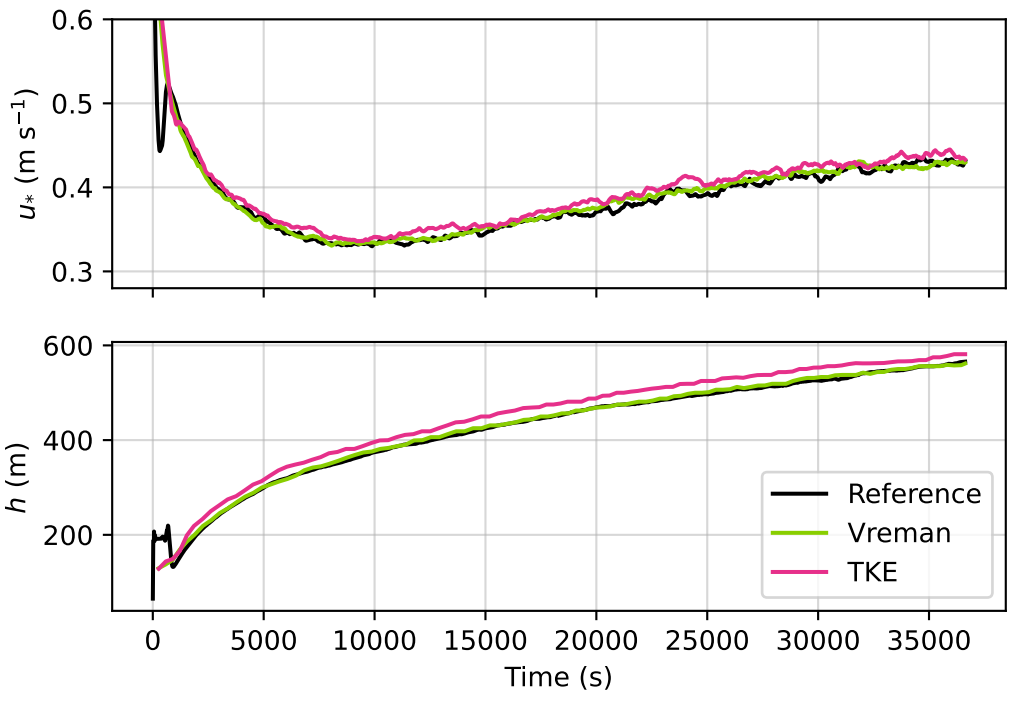
0.6
0.5
0.4
0.3
u_* (m s^{-1})
600
400
200
h (m)
Reference
Vreman
TKE
0
5000
10000
15000
20000
25000
30000
35000
Time (s)

Figure4.

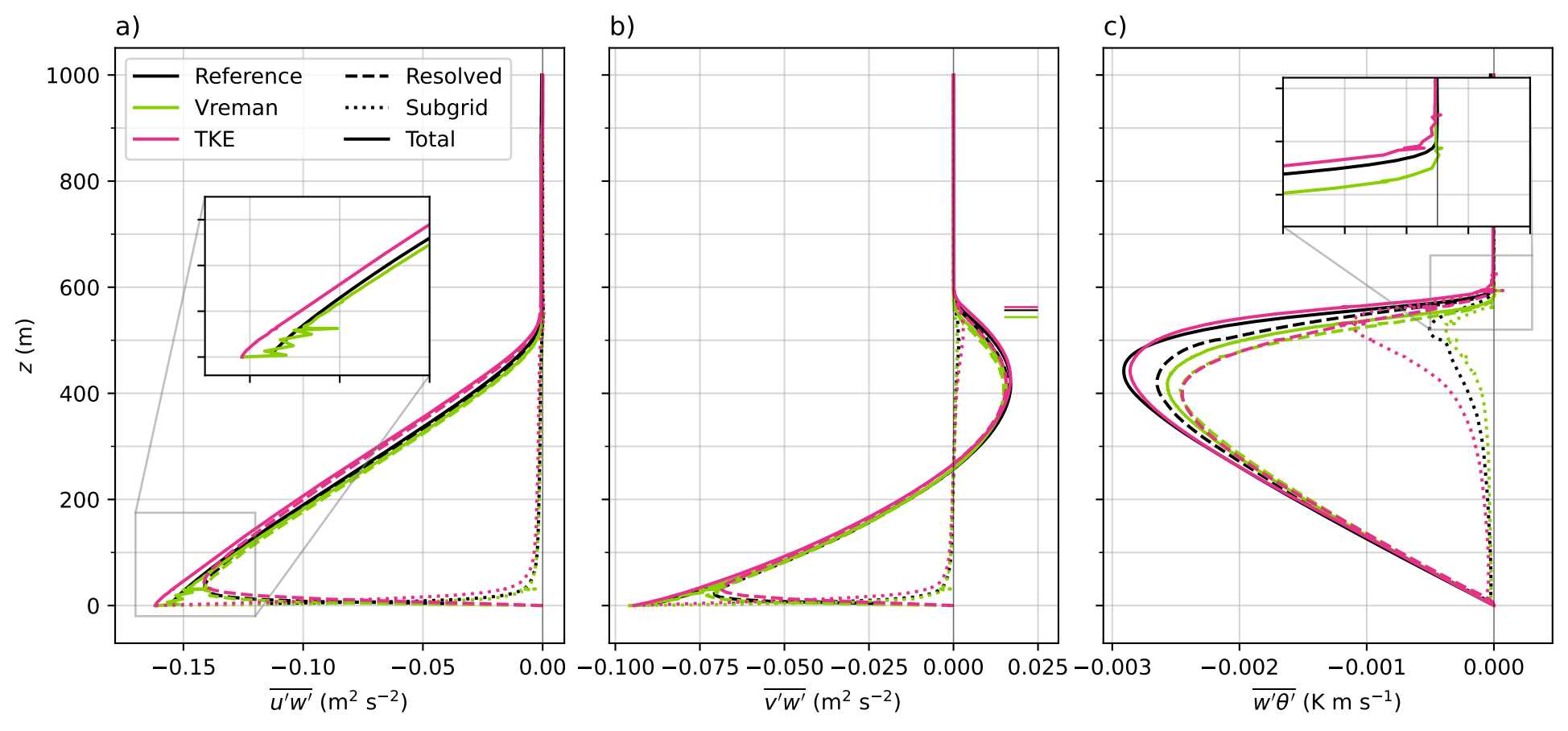
a)
b)
c)
Reference
Vreman
TKE
Resolved
Subgrid
Total
z (m)
1000
800
600
400
200
0
−0.15
−0.10
−0.05
0.00
−0.100
−0.075
−0.050
−0.025
0.000
0.025
−0.003
−0.002
−0.001
0.000
$\overline{u'w'}$ (m^2 s^{-2})
$\overline{v'w'}$ (m^2 s^{-2})
$\overline{w'\theta'}$ (K m s^{-1})

Figure5.

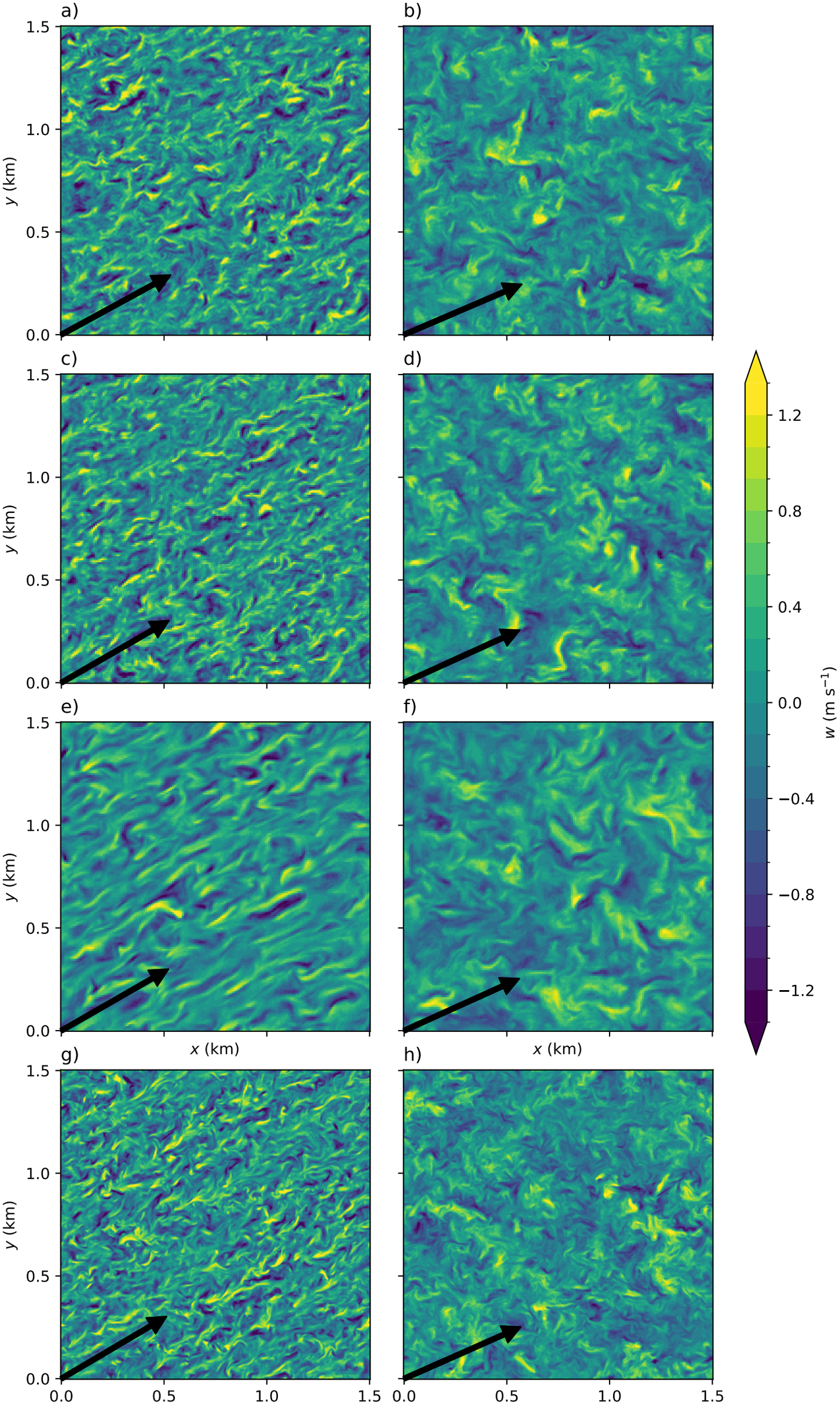
a)
b)
c)
d)
e)
f)
g)
h)
y (km)
x (km)
0.0
0.5
1.0
1.5
w (m s−1)
1.2
0.8
0.4
0.0
−0.4
−0.8
−1.2

Figure6.

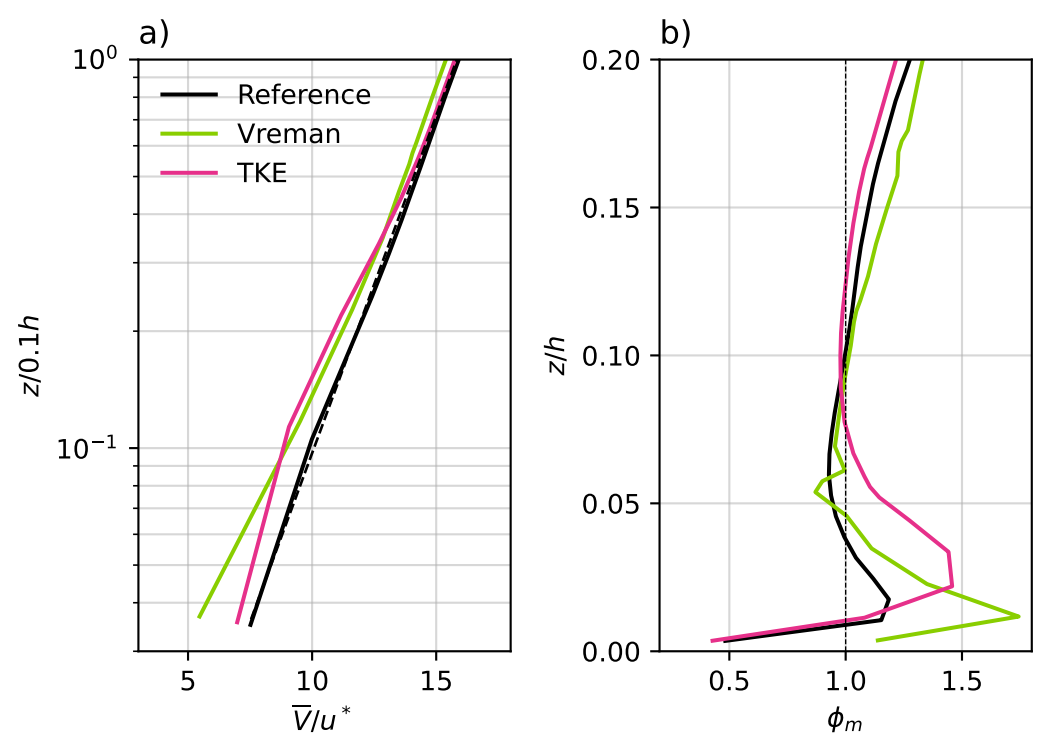
a)
b)
Reference
Vreman
TKE
10^0
10^{-1}
$z/0.1h$
$\overline{V}/u^*$
5
10
15
0.20
0.15
0.10
0.05
0.00
z/h
ϕ_m
0.5
1.0
1.5

Figure7.

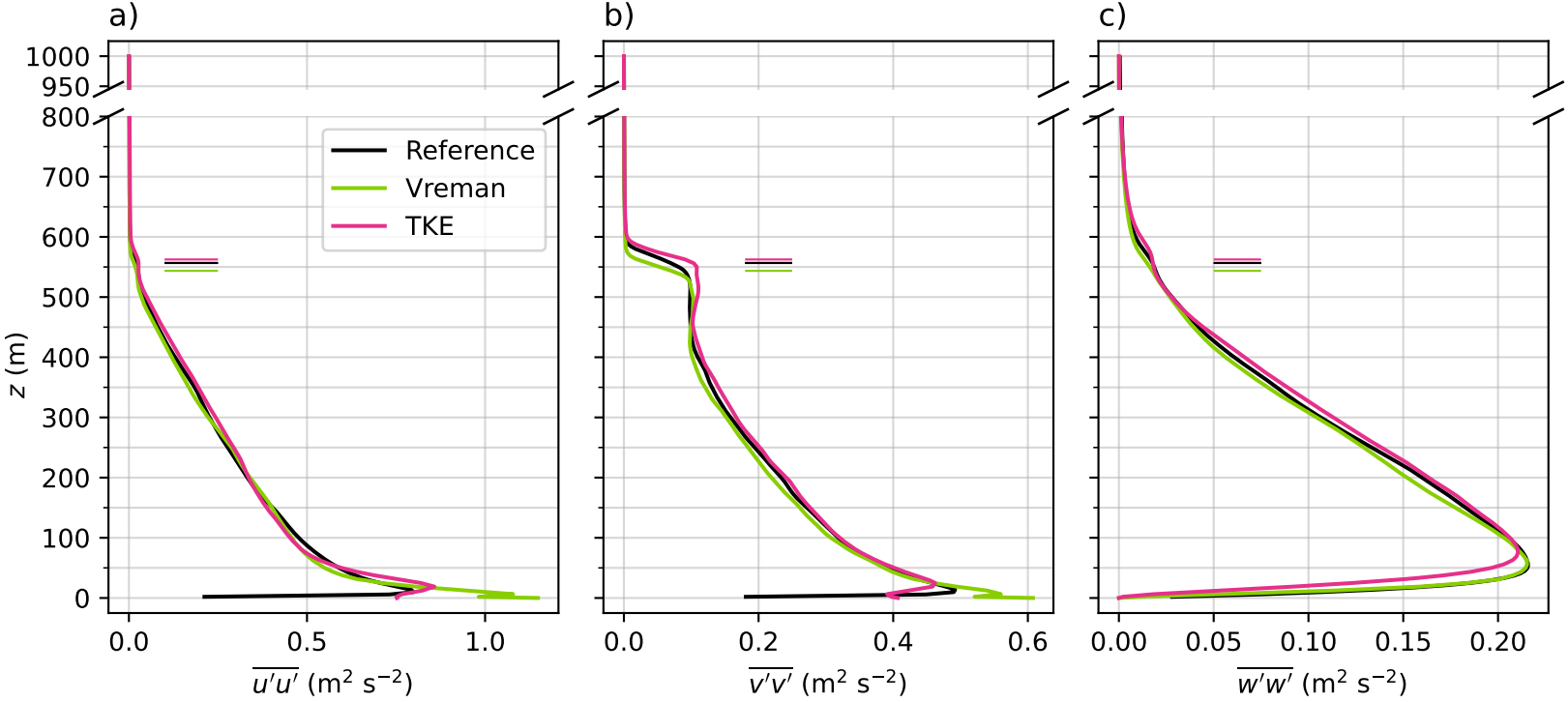
a)
b)
c)
Reference
Vreman
TKE
z (m)
1000
950
800
700
600
500
400
300
200
100
0
0.0
0.5
1.0
0.2
0.4
0.6
0.00
0.05
0.10
0.15
0.20
$\overline{u'u'}$ (m^2 s^{-2})
$\overline{v'v'}$ (m^2 s^{-2})
$\overline{w'w'}$ (m^2 s^{-2})

Figure8.

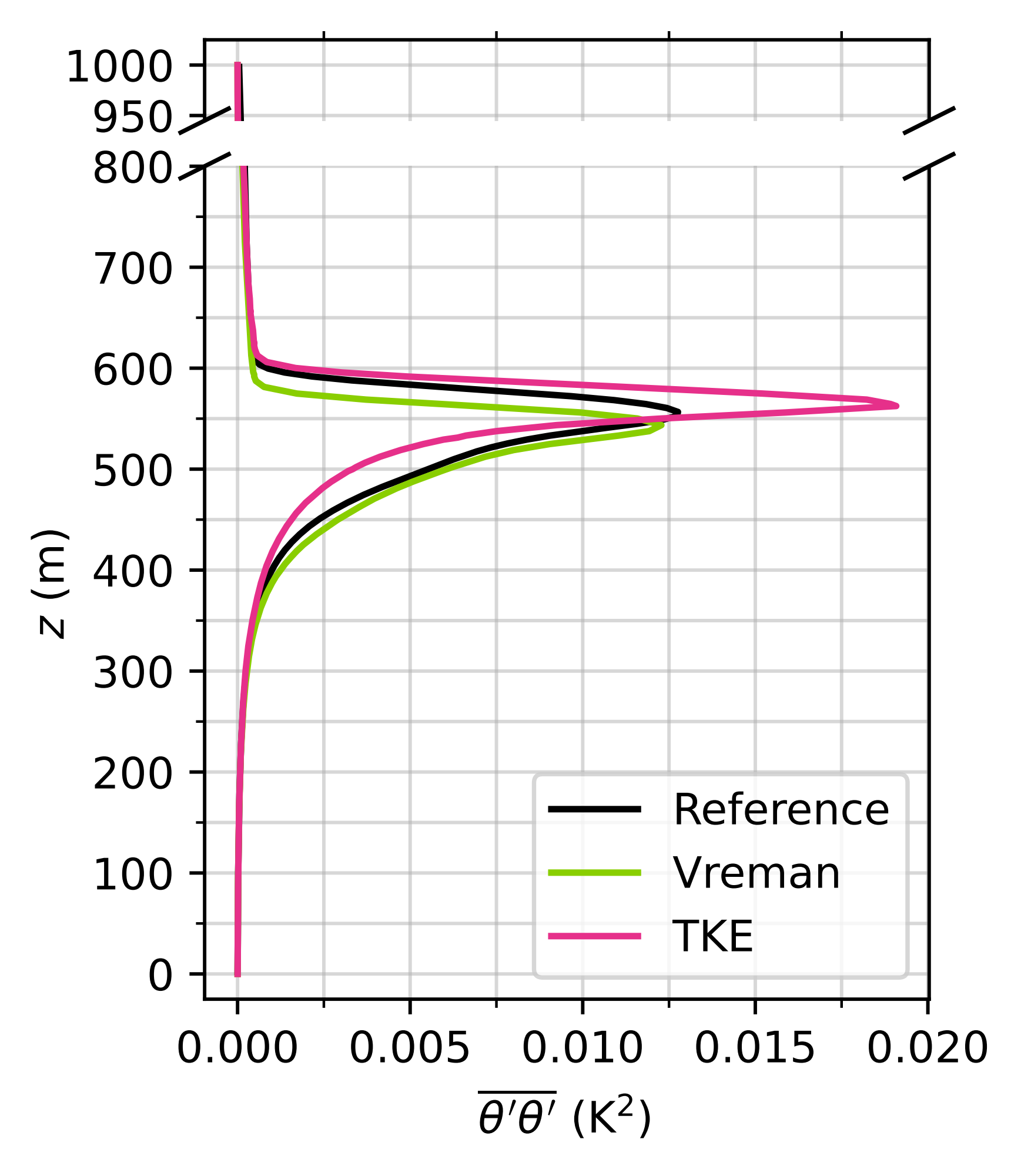
1000
950
800
700
600
500
400
300
200
100
0
z (m)
0.000
0.005
0.010
0.015
0.020
$\overline{\theta'\theta'}$ (K^2)
Reference
Vreman
TKE

Figure9.

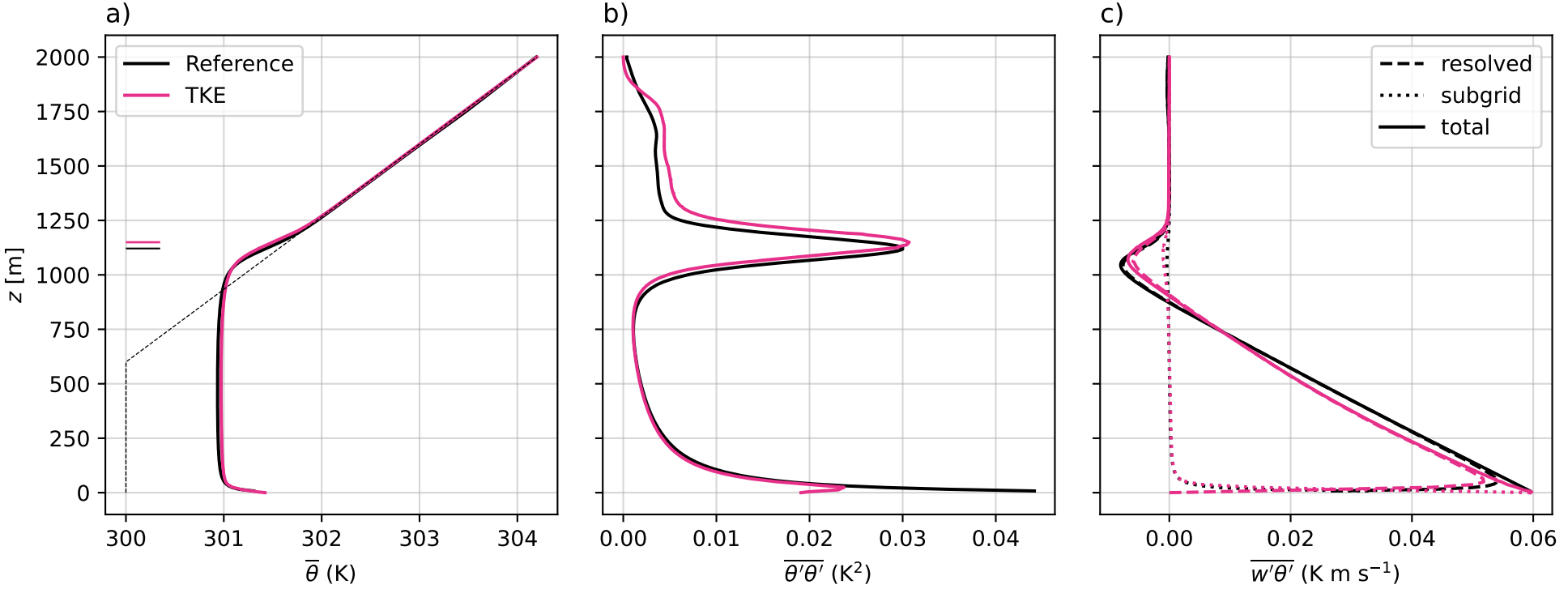
a)
b)
c)
Reference
TKE
resolved
subgrid
total
z [m]
2000
1750
1500
1250
1000
750
500
250
0
300
301
302
303
304
$\overline{\theta}$ (K)
0.00
0.01
0.02
0.03
0.04
$\overline{\theta'\theta'}$ (K^2)
0.00
0.02
0.04
0.06
$\overline{w'\theta'}$ (K m s^{-1})

Figure10.

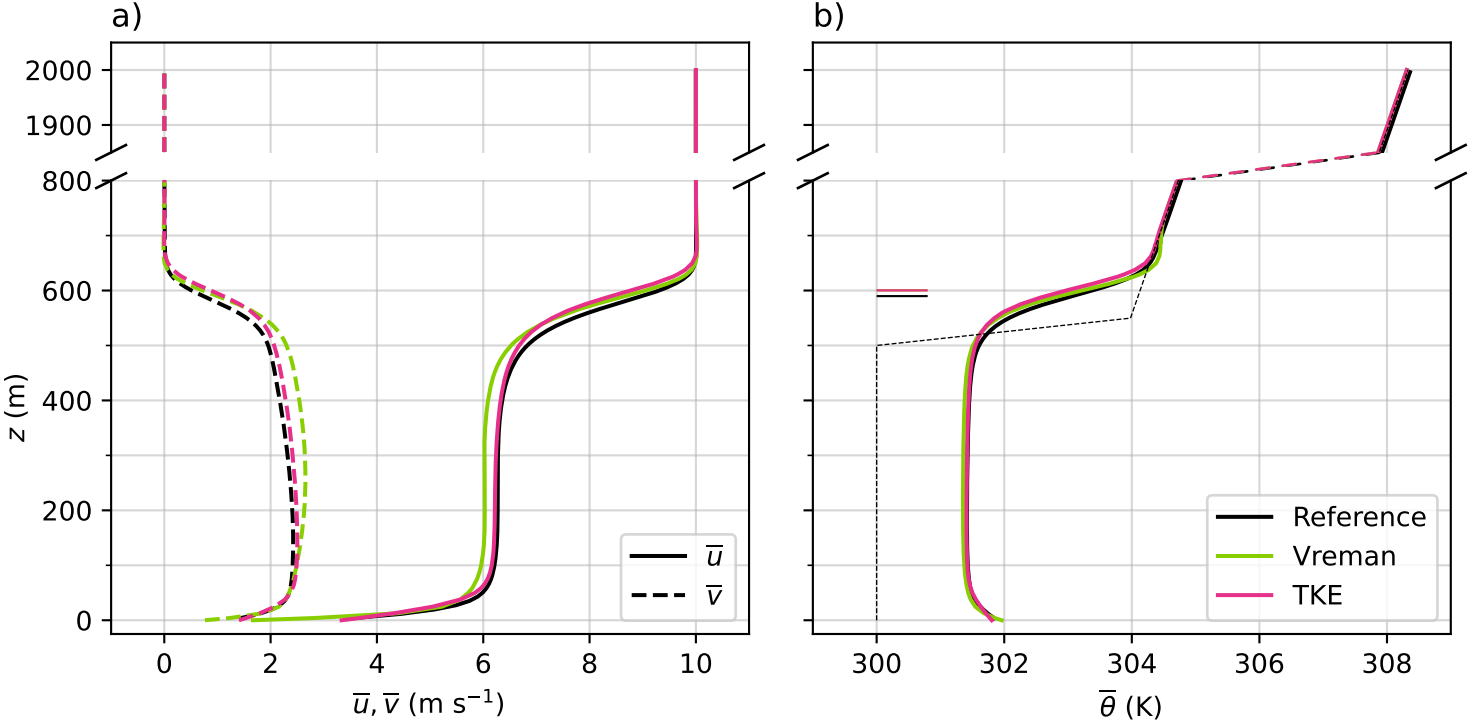
a)
b)
2000
1900
800
600
400
200
0
z (m)
0
2
4
6
8
10
$\overline{u}, \overline{v}$ (m s^{-1})
$\overline{u}$
$\overline{v}$
300
302
304
306
308
$\overline{\theta}$ (K)
Reference
Vreman
TKE

Figure11.

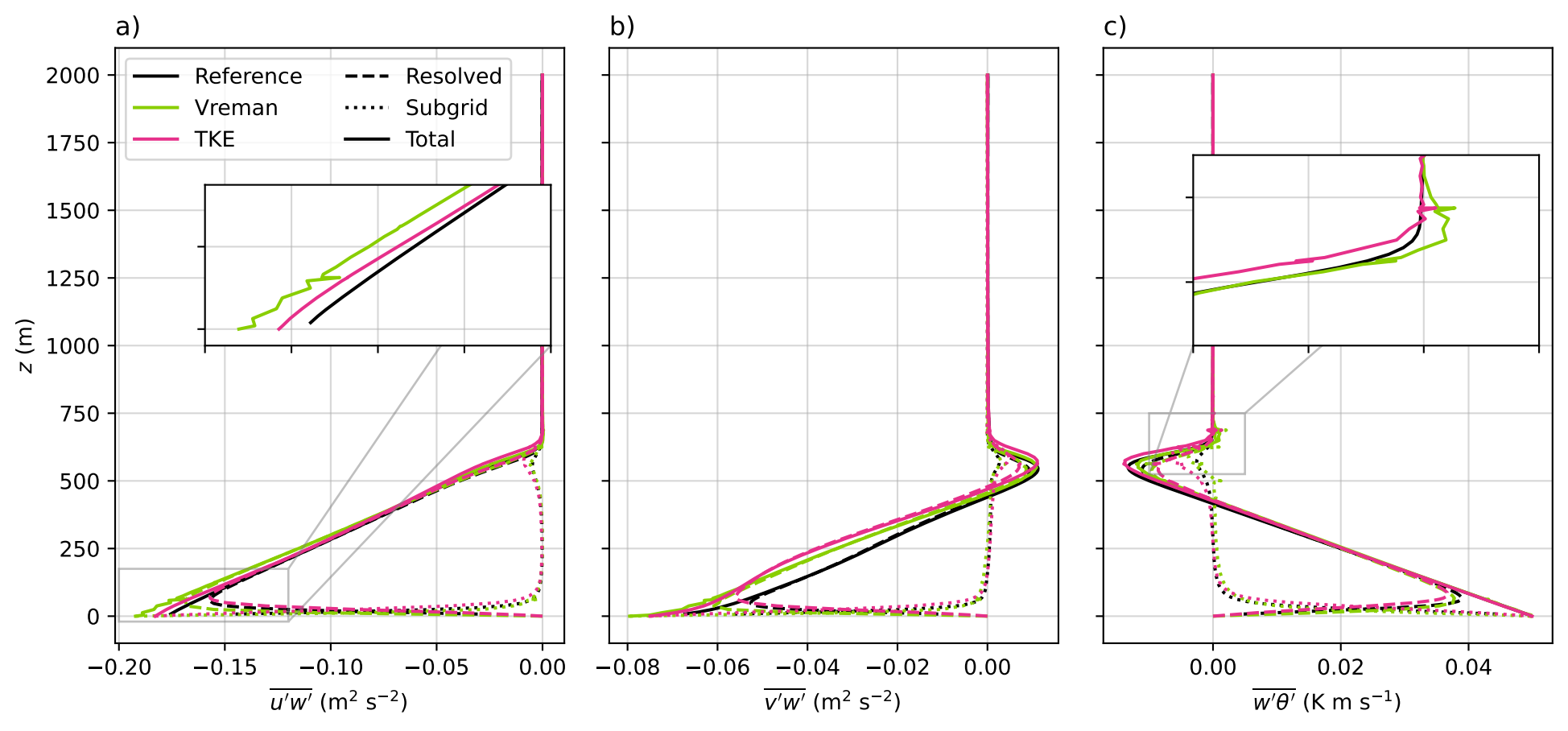
a)
b)
c)
Reference
Vreman
TKE
Resolved
Subgrid
Total
z (m)
2000
1750
1500
1250
1000
750
500
250
0
−0.20
−0.15
−0.10
−0.05
0.00
−0.08
−0.06
−0.04
−0.02
0.00
0.00
0.02
0.04
$\overline{u'w'}$ (m^2 s^{-2})
$\overline{v'w'}$ (m^2 s^{-2})
$\overline{w'\theta'}$ (K m s^{-1})

Figure12.

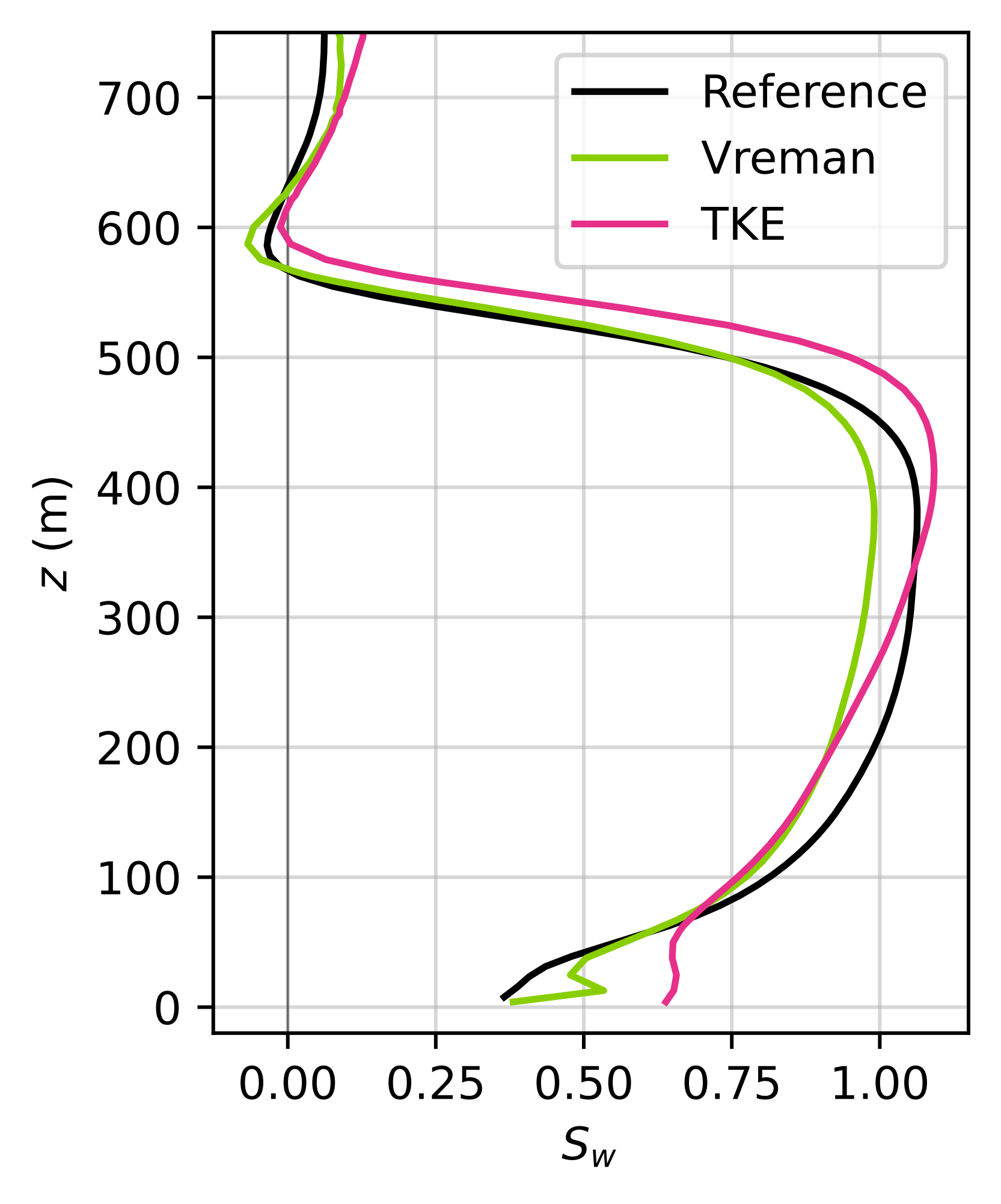
Reference
Vreman
TKE
700
600
500
400
300
200
100
0
z (m)
0.00
0.25
0.50
0.75
1.00
S_w

Figure13.

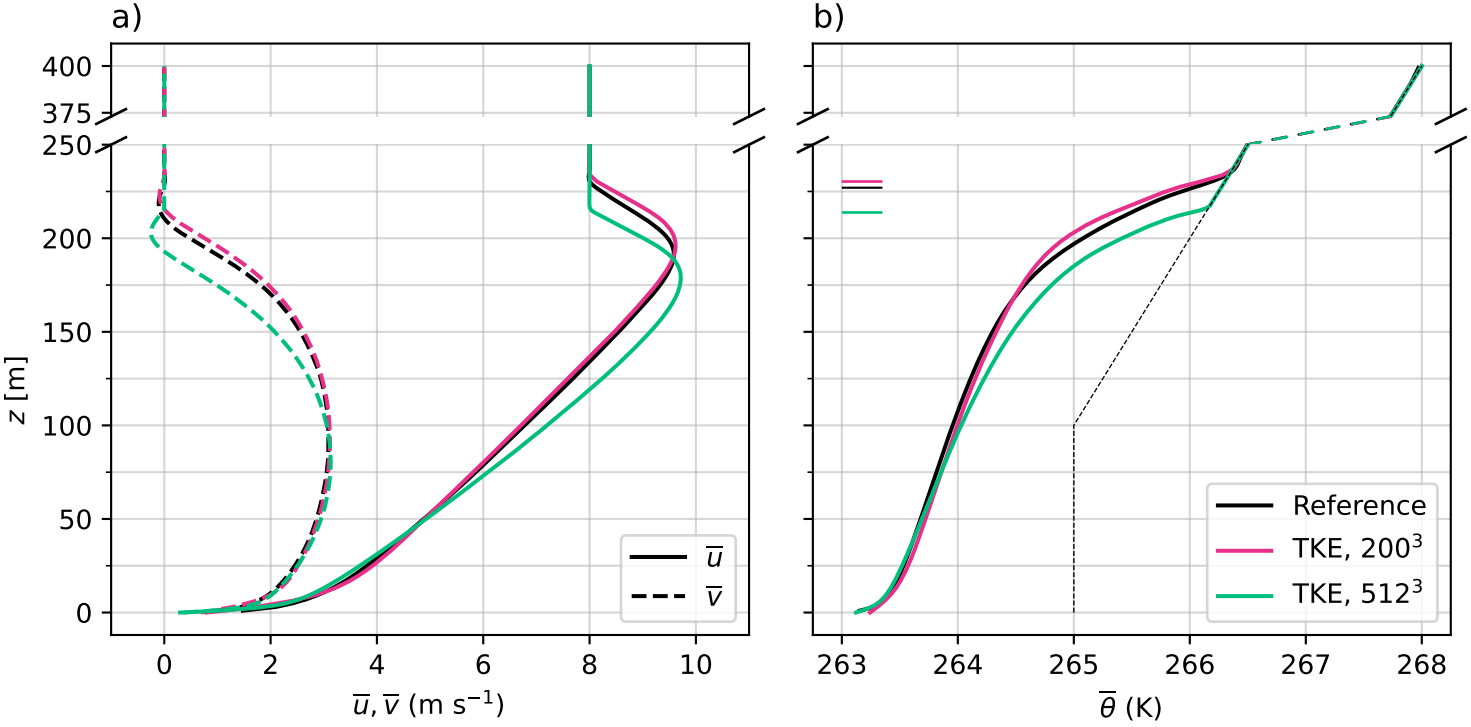
a)
b)
400
375
250
200
150
100
50
0
z [m]
0
2
4
6
8
10
$\overline{u}, \overline{v}$ (m s^{-1})
$\overline{u}$
$\overline{v}$
263
264
265
266
267
268
$\overline{\theta}$ (K)
Reference
TKE, 200^3
TKE, 512^3

Figure14.

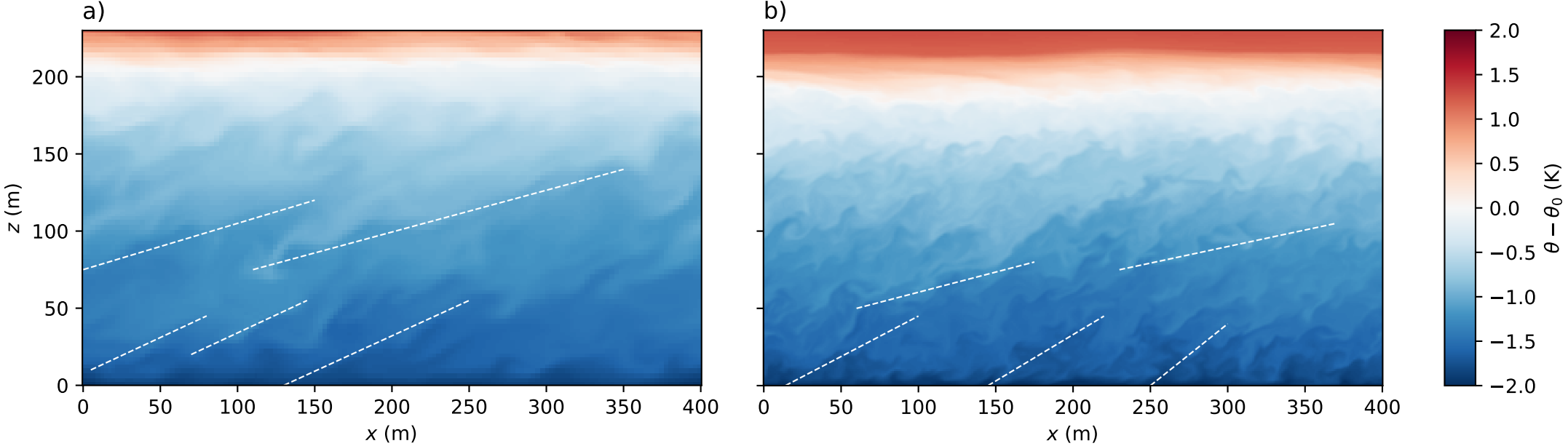
a)
b)
z (m)
x (m)
x (m)
0
50
100
150
200
250
300
350
400
2.0
1.5
1.0
0.5
0.0
−0.5
−1.0
−1.5
−2.0
θ − θ0 (K)

Figure15.

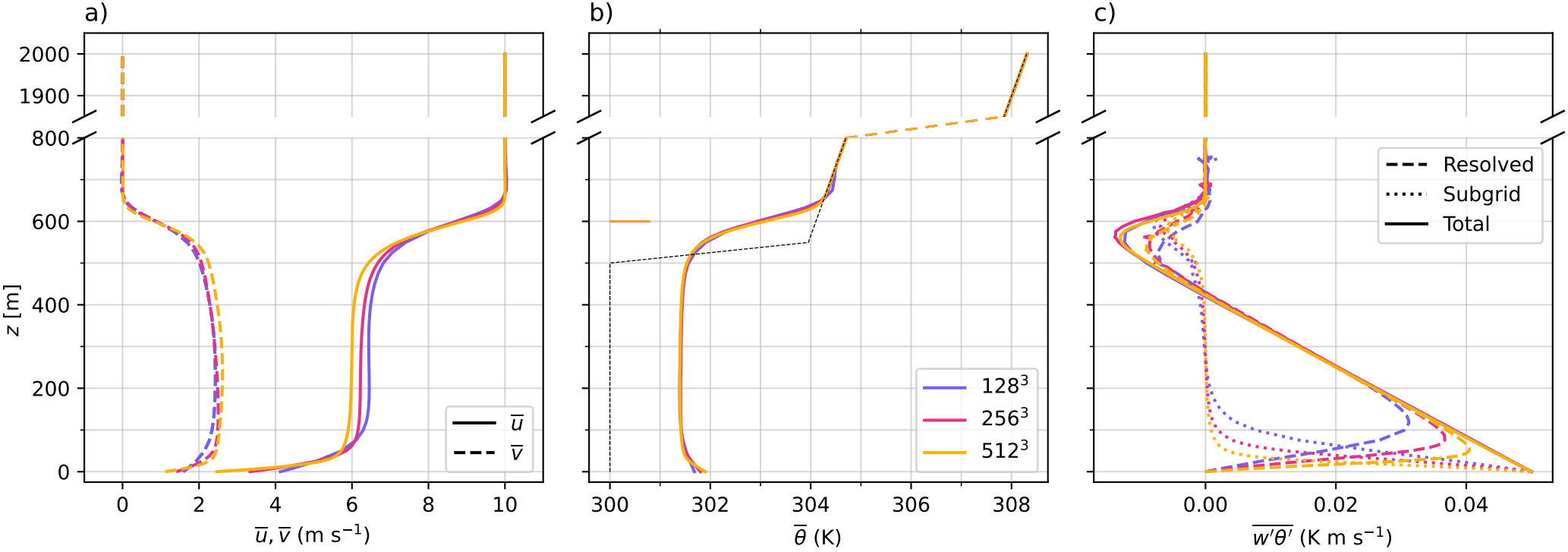
a)
b)
c)
2000
1900
800
600
400
200
0
z [m]
0
2
4
6
8
10
$\overline{u}, \overline{v}$ (m s^{-1})
$\overline{u}$
$\overline{v}$
300
302
304
306
308
$\overline{\theta}$ (K)
128^3
256^3
512^3
0.00
0.02
0.04
$\overline{w'\theta'}$ (K m s^{-1})
Resolved
Subgrid
Total

Figure16.

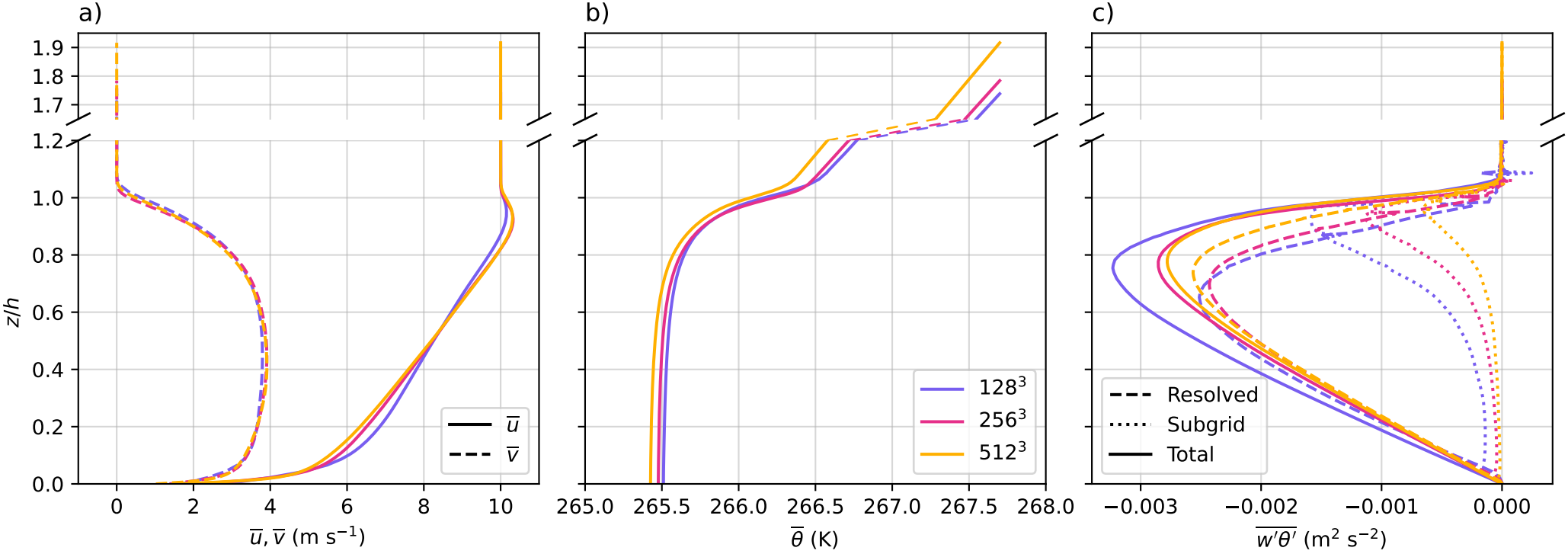
a)
b)
c)
z/h
1.9
1.8
1.7
1.2
1.0
0.8
0.6
0.4
0.2
0.0
0
2
4
6
8
10
$\overline{u}, \overline{v}$ (m s^{-1})
$\overline{u}$
$\overline{v}$
265.0
265.5
266.0
266.5
267.0
267.5
268.0
$\overline{\theta}$ (K)
128^3
256^3
512^3
−0.003
−0.002
−0.001
0.000
$\overline{w'\theta'}$ (m^2 s^{-2})
Resolved
Subgrid
Total

Figure17.

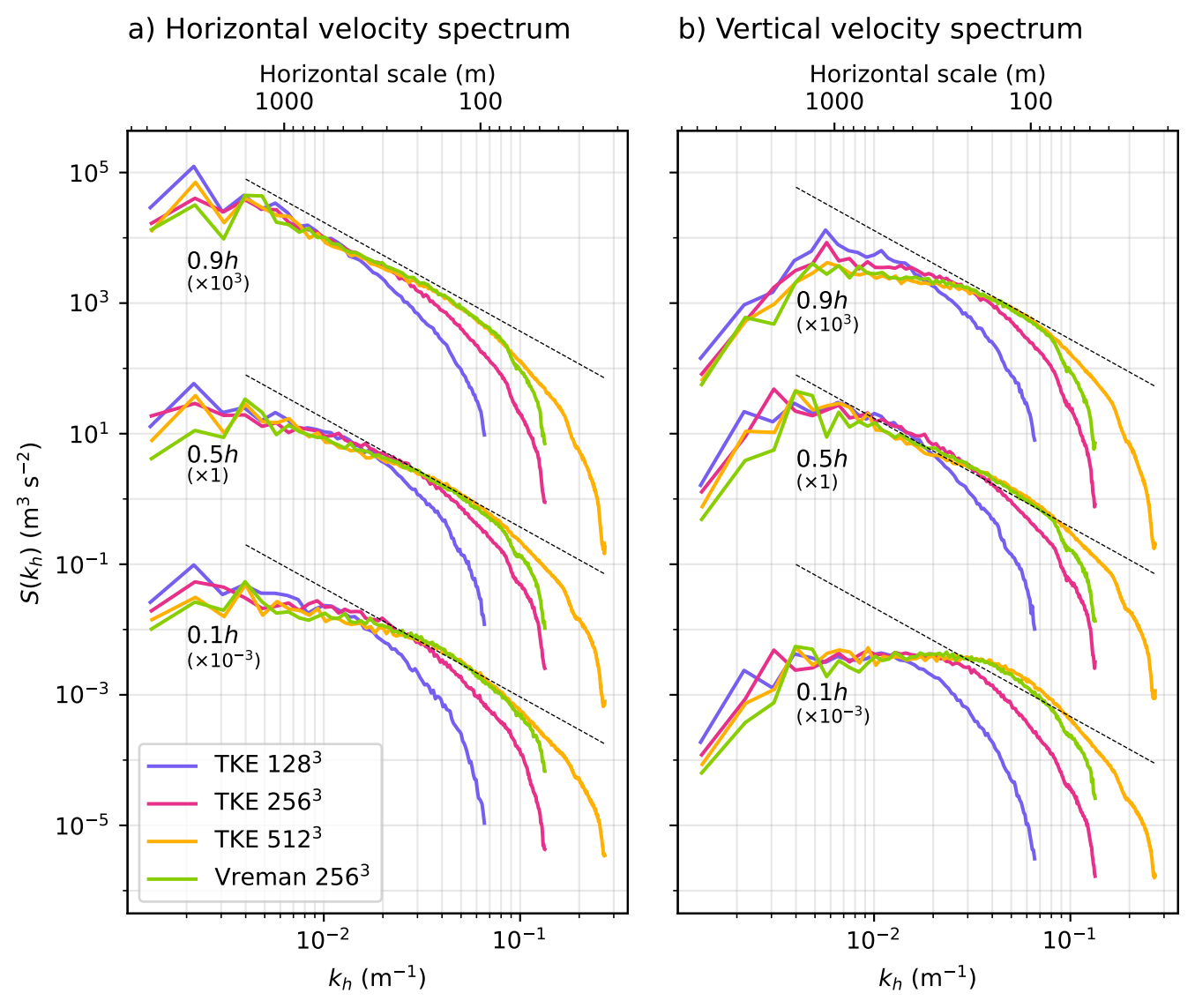
a) Horizontal velocity spectrum
b) Vertical velocity spectrum
Horizontal scale (m)
1000
100
10^5
10^3
10^1
10^{-1}
10^{-3}
10^{-5}
$S(k_h)$ (m^3 s^{-2})
0.9h
(×10^3)
0.5h
(×1)
0.1h
(×10^{-3})
TKE 128^3
TKE 256^3
TKE 512^3
Vreman 256^3
10^{-2}
10^{-1}
k_h (m^{-1})

Figure18.

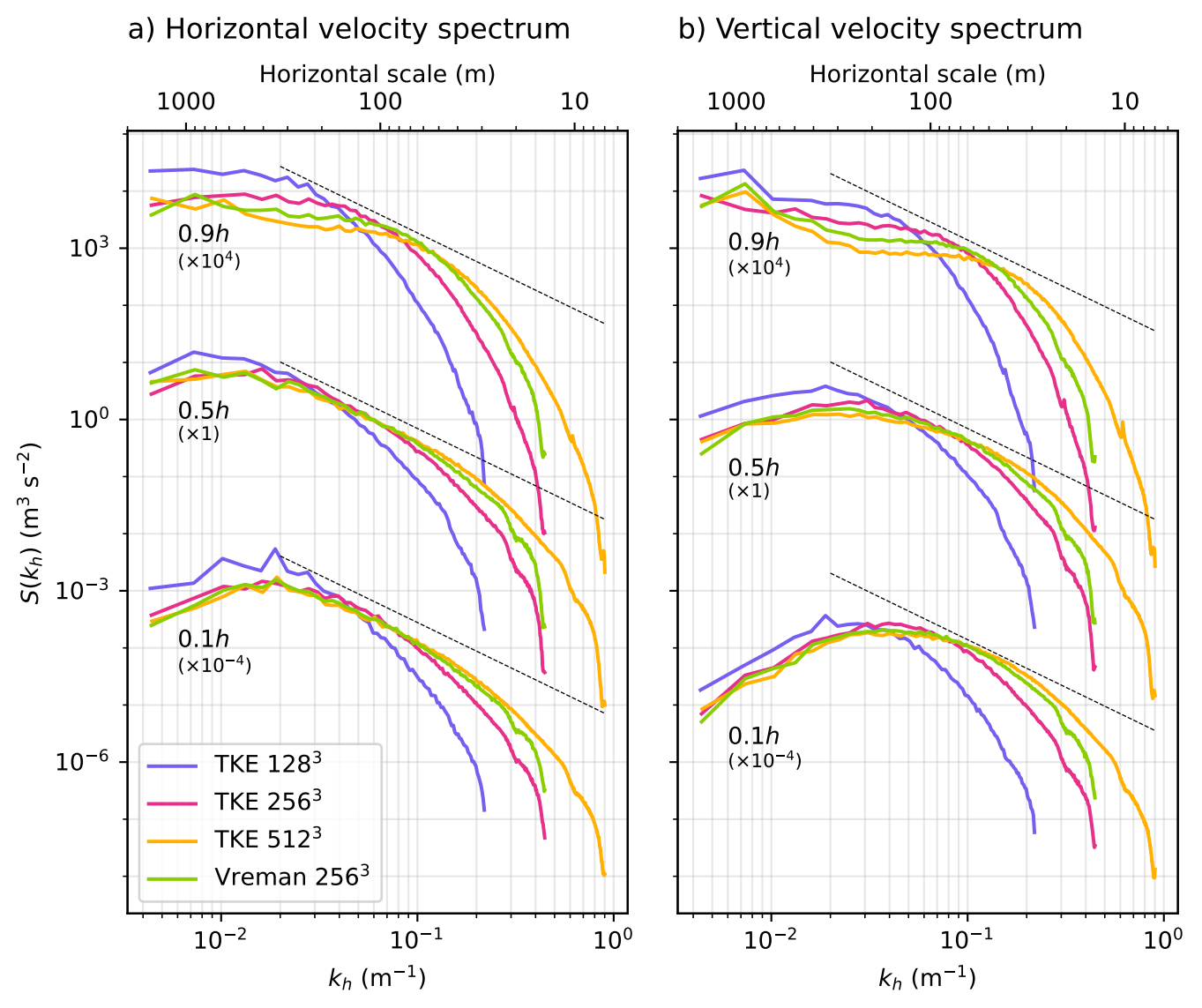
a) Horizontal velocity spectrum
b) Vertical velocity spectrum
Horizontal scale (m)
1000
100
10
$S(k_h)$ (m^3 s^{-2})
10^3
10^0
10^{-3}
10^{-6}
0.9h
(×10^4)
0.5h
(×1)
0.1h
(×10^{-4})
TKE 128^3
TKE 256^3
TKE 512^3
Vreman 256^3
10^{-2}
10^{-1}
10^0
k_h (m^{-1})

Figure19.

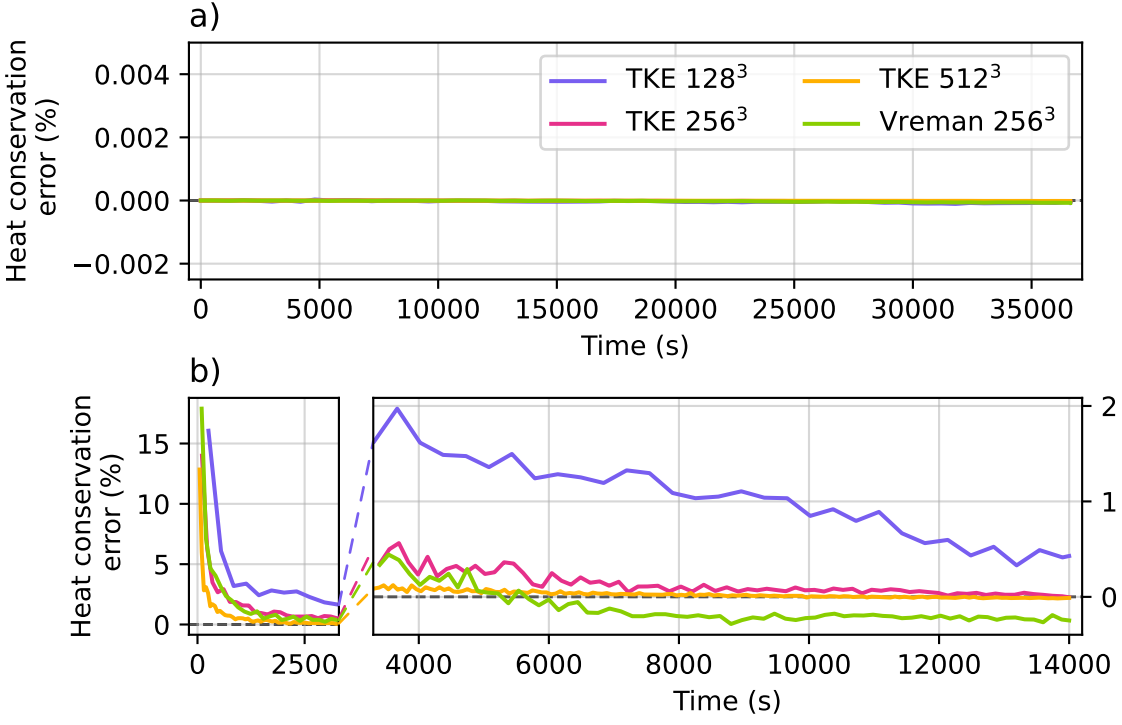
a)
Heat conservation error (%)
0.004
0.002
0.000
−0.002
TKE 128³
TKE 256³
TKE 512³
Vreman 256³
0
5000
10000
15000
20000
25000
30000
35000
Time (s)
b)
Heat conservation error (%)
15
10
5
0
0
2500
4000
6000
8000
10000
12000
14000
Time (s)
2
1
0

FigureB1.

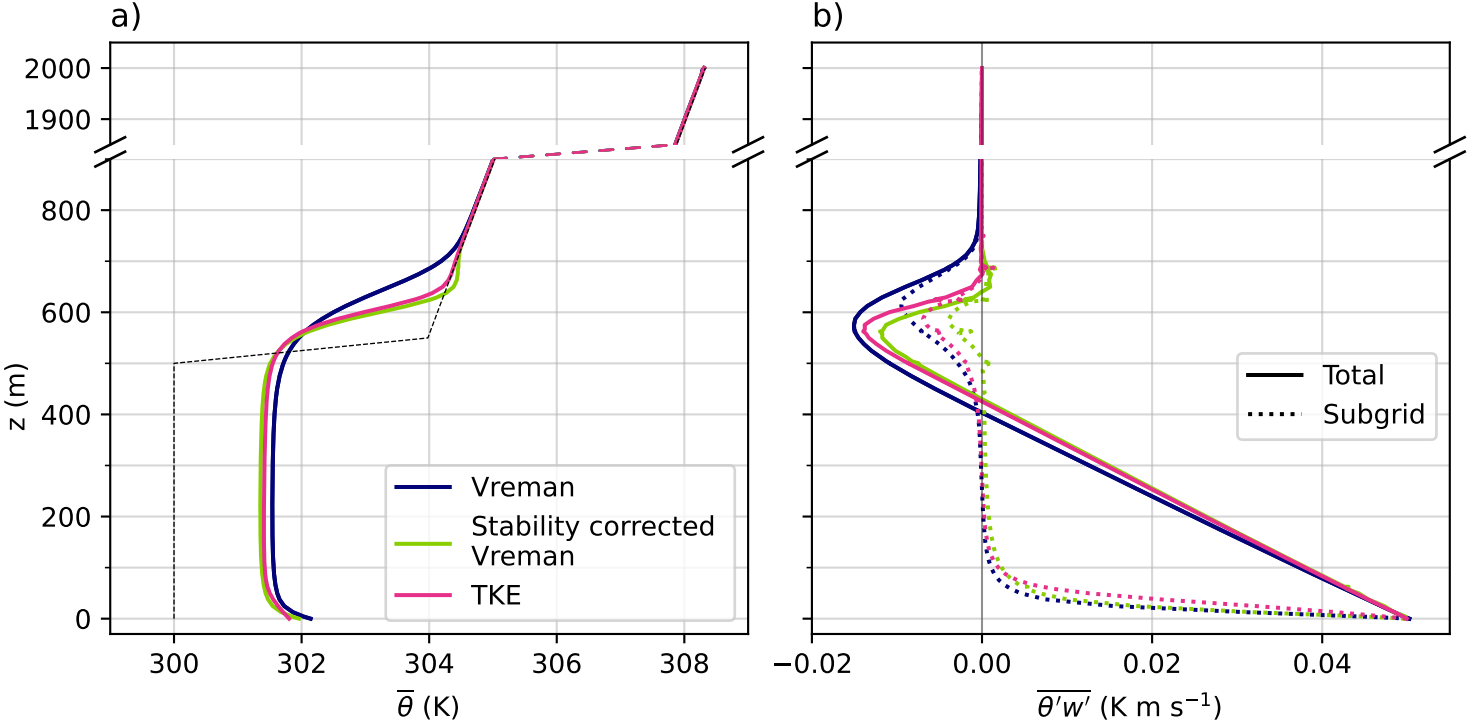
a)
b)
2000
1900
800
600
400
200
0
z (m)
300
302
304
306
308
$\overline{\theta}$ (K)
Vreman
Stability corrected Vreman
TKE
−0.02
0.00
0.02
0.04
$\overline{\theta' w'}$ (K m s^{-1})
Total
Subgrid

FigureB2.

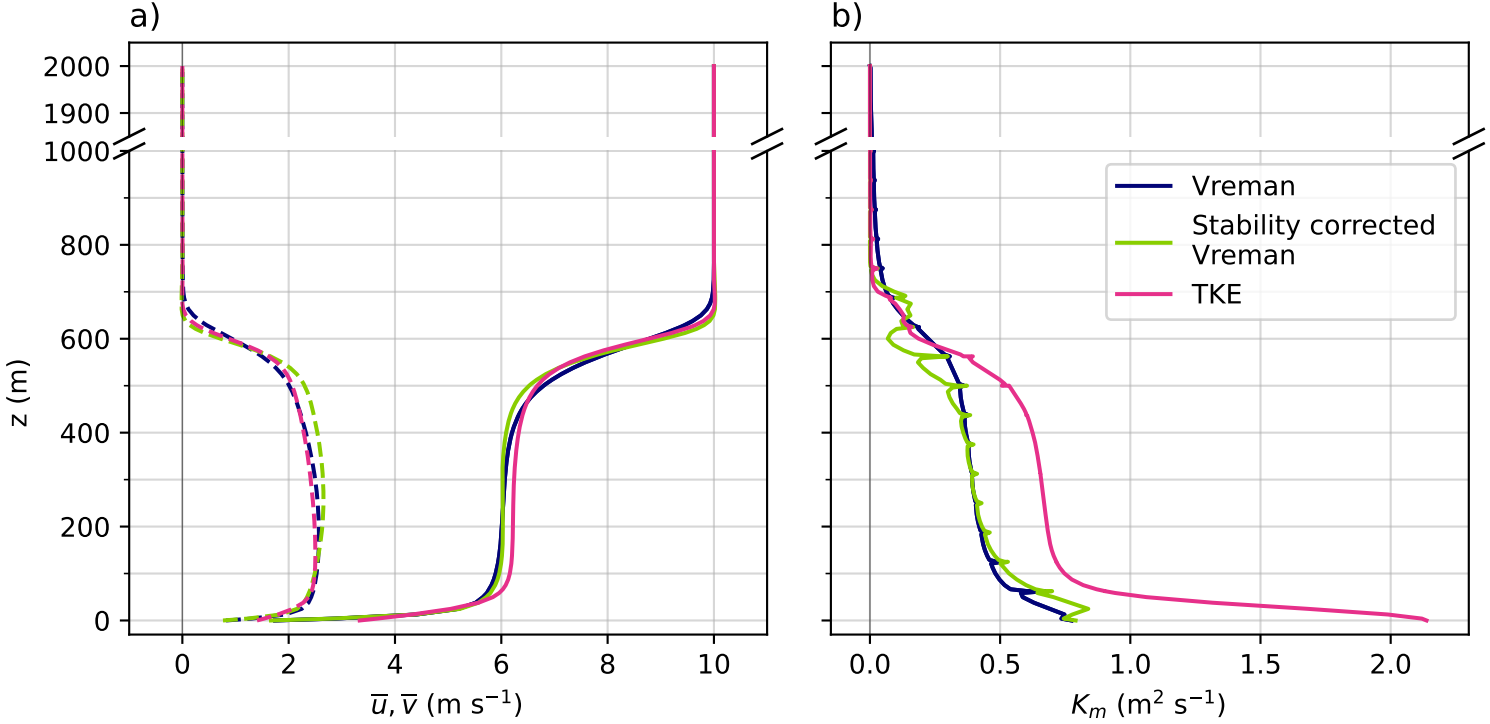
a)
b)
2000
1900
1000
800
600
400
200
0
z (m)
0
2
4
6
8
10
$\overline{u}, \overline{v}$ (m s^{-1})
0.0
0.5
1.0
1.5
2.0
K_m (m^2 s^{-1})
Vreman
Stability corrected Vreman
TKE